

AD-A064 089

YALE UNIV NEW HAVEN CONN DEPT OF ENGINEERING AND AP--ETC F/6 11/6
THE STUDY OF ALLOY SURFACES BY PLASMON EXCITATION.(U)
DEC 78 W D ROBERTSON, A HERZENBERG

N00014-76-C-0284

UNCLASSIFIED

NL

| OF |

AD
A064089

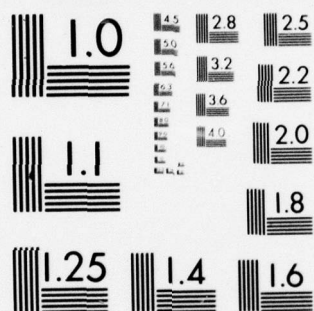


END

DATE
FILMED

4-79

DDC



MICROCOPY RESOLUTION TEST CHART
NATIONAL BUREAU OF STANDARDS-1963-A

DDC FILE COPY

ADA064089



LEVEL II

12

9 FINAL REPORT. 1 Oct 75 - 31 Aug 78

To

Office of Naval Research - Metallurgy Program

Contract No. SAR/N00014-76-C-0284

15

6 THE STUDY OF ALLOY SURFACES BY PLASMON EXCITATION.

DDC
RECEIVED
FEB 1 1979
C

Principal Investigators:

10 Professor W. D. Robertson
Professor Arvid Herzenberg

Assistant in Research:

Charles W. Tu

Period of Research:

October 1, 1975 to August 31, 1978

11 14 Dec 78

12 68 p.

Report, Abstracted from the Dissertation Presented to the Faculty of the Graduate School, Yale University, by Charles W. Tu for the Ph.D.

Arvid Herzenberg
Arvid Herzenberg
Professor of Engineering & Applied Science

W. D. Robertson
W. D. Robertson
Professor of Applied Science

December 14, 1978

This document has been approved for public release and sale; its distribution is unlimited.

DEPARTMENT OF ENGINEERING
AND APPLIED SCIENCE

YALE UNIVERSITY

79 01 16 021

400 987

el

TABLE OF CONTENTS

	Page
INTRODUCTION	
Motivation	1
Energy Loss Spectroscopy at Glancing Incidence	3
Scope of the Present Investigation	5
Surface Plasmons	5
Previous Experimental Results	8
The Effect of Impurity Adsorption on Surface Plasmons	10
DESIGN AND OPERATING CHARACTERISTICS OF APPARATUS	12
Design Considerations	12
Vacuum System	13
Electron Gun	14
Energy Analyzer	14
Detection Electronics	15
Sample Preparation and Cleaning	20
Alignment	21
Energy Resolution	23
Angular Resolution	25
EXPERIMENTAL PROCEDURE	28
Glancing Incidence	28
Momentum Determination	29
EXPERIMENTAL RESULTS	33
Energy Loss Spectra	33
Comparison with Spectra Obtained from ILEED	39
COMPARISON WITH THEORETICAL DISPERSION RELATIONSHIPS	42
CONCLUSIONS	50
APPENDIX - OXYGEN ADSORPTION ON AL(100)	51
Introduction	51
Experimental Procedure	51
Spectra from Adsorbed Oxygen	52
Discussion	59
CONCLUSIONS CONCERNING OXYGEN ADSORPTION	62
REFERENCES	63

ABSTRACT

The surface plasmon dispersion relation for the (100) surface plane of aluminum has been measured by electron energy loss spectroscopy at glancing incidence, which completely suppresses the volume plasmon and minimizes multiple scattering. The dispersion relationship, in powers of $k_{||} V_F / \omega_p$, is $\hbar\omega_{SP} = 10.34 (\pm 0.08) - 1.9 (\pm 0.6) k_{||} + 7(\pm 1) k_{||}^2$. This relationship compares favorably with the only other measurement (made by a different technique, ILEED) on a well characterized single crystal surface. The results of the two independent measurements disagree substantially with all of the numerous dispersion relationships which are computed for different models of the surface charge density profile and which employ different computational approximations. However, the negative sign of the linear coefficient (-1.9), which is related to the density fluctuation of surface plasmons, is established and it may be interpreted to mean that the maximum in the surface charge fluctuation occurs inside the metal, rather than symmetrically about the surface plane.

An appendix describes the effect of adsorbed oxygen on the energy loss spectra obtained from a clean surface. The surface plasmon peak at 10.3 eV is displaced by a new peak at 7.5 eV as oxygen exposure (torr-seconds) is increased. At large exposure of oxygen a broad peak appears at 20.6 eV. Plasmon dispersion was measured to $k_{||} = 0.33 \text{ \AA}^{-1}$ during oxygen exposure and it was found to be constant until the 10.3 eV plasmon peak disappears from the spectrum.

ABSTRACT for	
NTIS	Write Section <input checked="" type="checkbox"/>
DDG	Self Section <input type="checkbox"/>
UNANNOUNCED	<input type="checkbox"/>
JUSTIFICATION <i>Per letter on file</i>	
BY	
DISTRIBUTION/AVAILABILITY CODES	
Dist.	AVAIL. INT. OR SERIAL
79 01 16 02	A

INTRODUCTION

Motivation

Physical properties that depend on the electron distribution at a surface include the work function, the surface energy, surface plasmons and surface phonons. In the vicinity of the surface, the electron wave function has an exponential tail, which gives rise to a region of nonuniform electron density in the surface layer, Fig. 1. In the surface layer, the background charge is not compensated and a dipole layer is formed at the surface. This dipole layer in turn gives rise to a potential step, V_{dipole} , which is an important contribution to the work function ϕ .

The restoring electric field which sustains the surface plasma oscillation extends beyond the boundary of the specimen, in contrast to the volume plasma oscillation which is confined in the bulk material. The range of this field varies with the wave vector of surface plasmons; therefore, the surface plasmon dispersion relationship (SPDR) can probe the electron distribution at the surface. In addition, a surface plasmon can be affected by the state of the surface, for example, by the presence of a second component at the vacuum interface and by the crystal structure of the surface plane. Furthermore, the excitation of surface plasmons is important because the creation of surface plasmons is the principal inelastic process contributing to the short mean free path of electrons that makes surface analytical techniques possible.

We chose the (100) plane of aluminum as the sample for these measurements for several reasons. One is that Al is a nearly free electron metal and has been the subject of extensive theoretical studies. Furthermore,

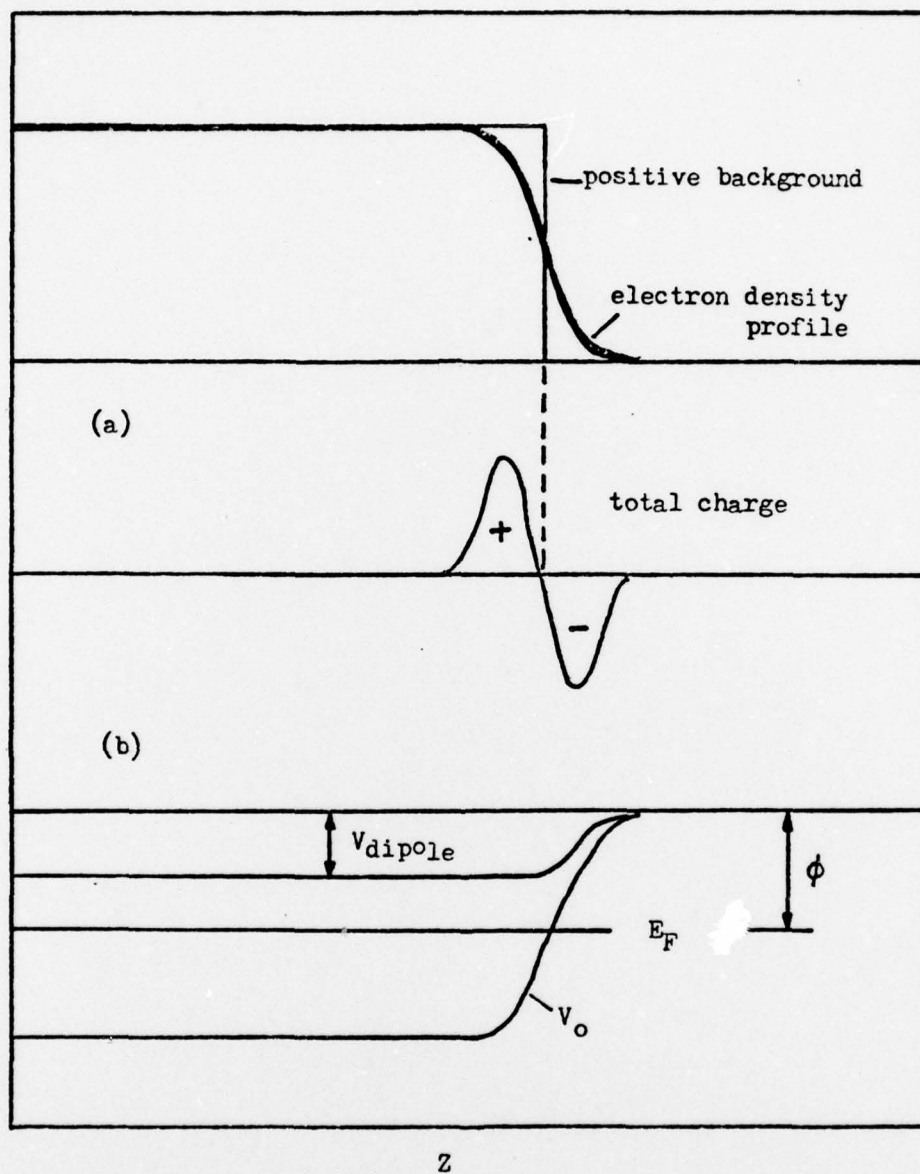


Fig. 1 (a) The electron density profile in a jellium model and the resultant dipole layer.

(b) The potential experienced by an electron in a metal, V_0 . E_F is the Fermi energy, ϕ is the work function, and V_{dipole} is the potential from the dipole layer.
(After Celli¹)

surface plasmons and volume plasmons in Al are well defined and identified. Another reason is that our laboratory has extensive LEED and AES experience in the structural properties and chemical composition of Al(100) and in the preparation of a clean Al(100) surface.

Energy Loss Spectroscopy at Glancing Incidence

Surface plasmons appear in a variety of physical situations, for example, as satellite lines in x-ray photoelectron spectroscopy (XPS), in electron and ion yield spectroscopy, in optical reflectance of solids, in energy loss spectra of fast electrons passing through thin films and of slow electrons reflecting from surfaces.

To maximize the effects from the surface and to minimize the complicating factor of multiple scattering in the bulk material, the incident electrons are directed to the surface at a glancing angle, θ_0 . Figure 2 shows the geometry of the experimental arrangement. The sample normal is the z-axis, and x- and y-axis are along the $\langle 11 \rangle$ crystallographic directions, which are the most closely packed directions in the (100) plane.

To simplify theoretical analysis, the analyzer is situated in the plane of incidence, defined by the direction of the incoming electrons and the normal to the surface. The penetration depth is therefore proportional to $\lambda \sin \theta_0$, where λ is the mean free path of the electron; the information depth is roughly half of this because the electrons must be reflected from the surface to be detected. Only the first and the second layers of atoms on the surface are involved in the scattering process when $\theta_0 \leq 10^\circ$ and the intensity of the surface effect increases by $1/\sin \theta_0$ at glancing incidence, relative to normal incidence.

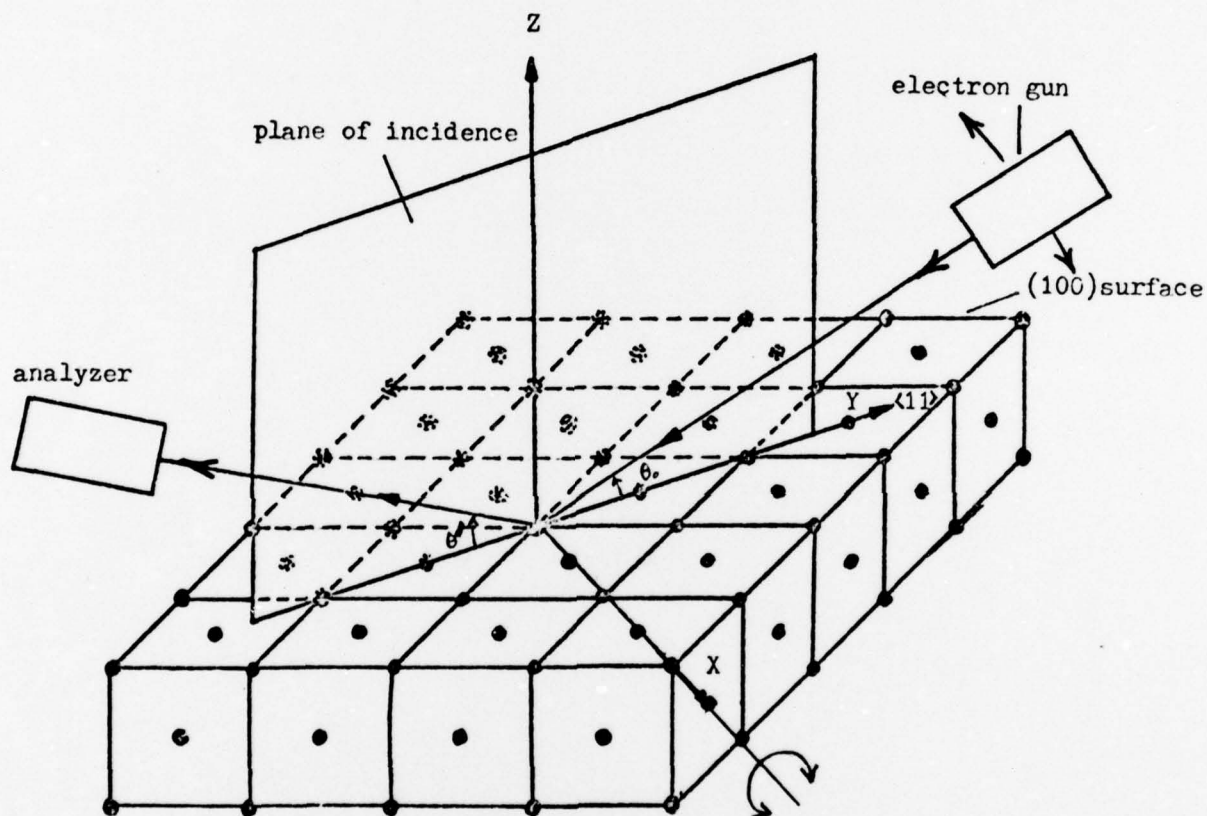


Fig. 2

The experimental geometry in the energy loss spectroscopy. The plane of incidence is defined by the direction of the incoming electrons and the normal of the surface (Z). θ and θ' are measured from the surface. The Y axis is along the $\langle 111 \rangle$ direction of the crystal lattice. The aluminum crystal structure is fcc.

Scope of the Present Investigation

To study properties of surface plasmons in angle-resolved, electron energy loss spectroscopy at glancing incidence, we have designed and built a spectrometer system which is housed in an ultra-high vacuum chamber. The spectrometer system consists of an electron gun, a rotating sample holder, and an energy analyzer.

We first investigate the clean aluminum surface, measuring the SPDR and comparing it with various theoretical calculations.

In the course of measuring SPDR on the clean sample, we found that SPDR is a sensitive function of the cleanliness (oxygen) of the sample. To evaluate the sensitivity to oxygen adsorption, plasmon spectra were obtained as a function of oxygen concentration, temperature and time.

Surface Plasmons

We first define what is meant by a collective excitation as compared to a single particle excitation. When the mutual influence of Coulomb interactions among the valence electrons in a solid is small, the excitation spectrum of the valence electrons can be characterized by a set of one particle energy differences, corresponding to electronic transitions within the same band or from one band to another. When such transitions are excited by incident electrons we are dealing with energy transfer to a single valence electron, namely, a single particle energy loss.

However, in many cases, the Coulomb interaction between the valence electrons is strong and markedly influences the excitation spectrum of the system. The valence electrons as a result can carry out collective oscillations at high frequencies, which depend only on the electron charge, mass

and density in the solid. When an electron excites such collective oscillations, we are dealing with energy transfer to a number of electrons moving cooperatively. The collective oscillation resembles closely the natural density oscillation of a charged fluid--a plasma, studied by Langmuir in the 1920's. Bohm and Pines² in 1952 proposed the term plasmon to designate the quantum of this collective oscillation in a solid.

Surface charge density oscillations can also occur at the boundary of a solid (or liquid) and the quantum of such oscillations is a surface plasmon, predicted by Ritchie³ in 1957 in analyzing the energy loss spectra of fast electrons through thin films. Powell and Swan⁴ subsequently verified the existence of surface plasmons in Al and Mg.

Many theoretical papers⁵⁻⁷ have confirmed that at $k_{||} = 0$ limit (neglecting retardation) the surface plasmon frequency is the classical frequency, $\omega_p / \sqrt{2}$, independent of the surface potential profile. The observation of the limiting frequency, therefore, contains no information about the surface properties, and one has to study the behavior of surface plasmons at larger $k_{||}$ ($\sim 0.1 \text{ \AA}^{-1}$). However, at much larger $k_{||}$, or shorter wavelength, the plasmons of volume and surface origins lose their collective character when their wavelength is comparable to the mean distance between electrons. Thus, the significant range in which the surface structure and the electron density profile is probed is $0.1 \text{ \AA}^{-1} < k_{||} < 0.6 \text{ \AA}^{-1}$, Fig. 3.

More precisely, if the phase velocity, ω_p / k , of the volume or surface plasma waves reaches the velocity of the electrons, energy transfer takes place. The plasmons are damped by losing energy to the electrons. In an electron gas the critical wave vector k^c for the existence of surface plasmons is therefore $\sim \omega_p / v_F$, where v_F is the Fermi velocity of the electrons.

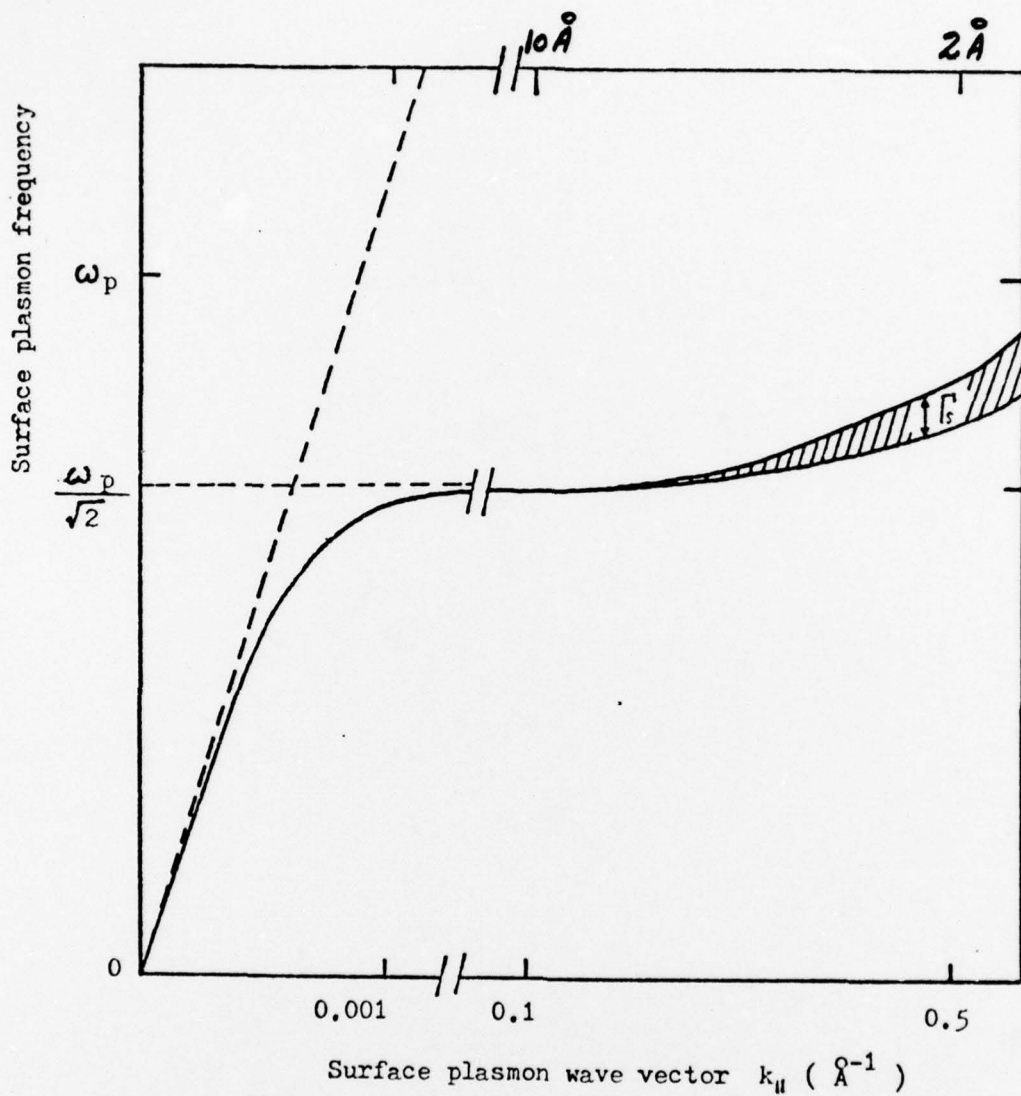


Fig. 3

A schematic representation of the behavior of surface plasmons in the long wavelength region and the short wavelength region. Γ_s represents the damping of surface plasmons.

Hence, for $0.1 \text{ \AA}^{-1} < k_{\parallel} \ll k^c \sim 1 \text{ \AA}^{-1}$ the surface plasmon dispersion relation (SPDR) can be expanded in powers of $k_{\parallel} v_F / \omega_p$:

$$\omega_s(k_{\parallel}) = \frac{\omega_p}{\sqrt{2}} \left[1 + (A_1 + iA_2) \frac{k_{\parallel} v_F}{\omega_p} + (B_1 + iB_2) \left(\frac{k_{\parallel} v_F}{\omega_p} \right)^2 + \dots \right] \quad (1)$$

Harris and Griffin⁸ have shown that within the quantum-mechanical random-phase-approximation (RPA), the linear coefficient A_1 is due to structure in the surface and is related to the charge dipole associated with the density fluctuation of surface plasmons. The sign of A_1 depends on where the surface plasmon charge fluctuation, which is strongly peaked near the surface, is located with respect to the unperturbed density profile $n_0(z)$, as shown in Fig. 4.

Many calculations exist for the SPDR in RPA, hydrodynamic approximation, or semiclassical approximation, using model surface potentials ranging from infinite barrier, step function, diffuse profile, trapezoidal shape to a self-consistent surface potential in jellium models. These calculations and the Harris-Griffin relation will be discussed and compared with the experimental data.

Previous Experimental Results

Kloos and Raether⁹, in their high energy (50 keV) electron transmission experiment, measured the SPDR for an aluminum film up to $k_{\parallel} = 0.28 \text{ \AA}^{-1}$ and observed no change in the surface plasmon energy. More recently, Krane and Raether¹⁰ extended that measurement to $k_{\parallel} = 0.47 \text{ \AA}^{-1}$ and observed an increase in the surface plasmon energy at higher k_{\parallel} . Duke and his coworkers have extracted the SPDR for Al(100)¹¹ and Al(111)¹²⁻¹⁴ crystal planes from

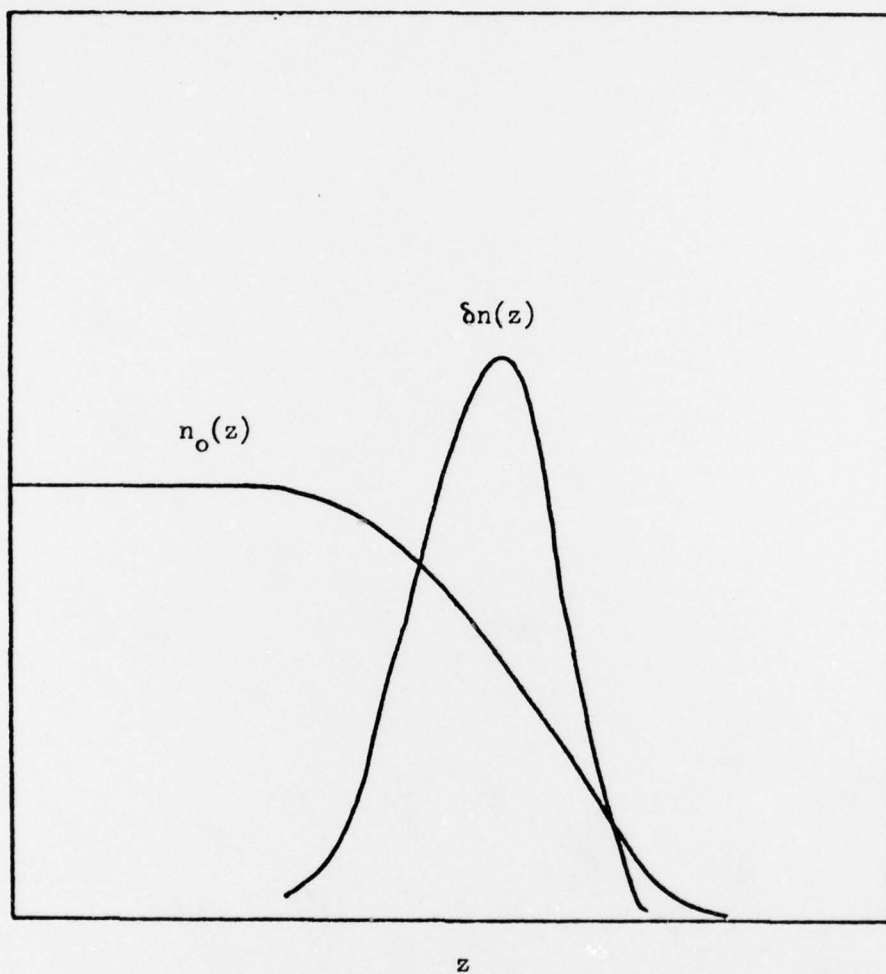


Fig. 4

A schematic representation of the unperturbed static electron density profile $n_0(z)$, and the charge oscillation due to surface plasmon $\delta n(z)$. (After Harris and Griffin²³)

the inelastic low energy (150 eV) electron diffraction (ILEED) data taken by Porteus and Faith¹⁵⁻¹⁷ and Wendelken and his coworkers¹⁸.

In the high energy electron transmission method, the momentum of the surface plasmon $k_{||}$ can be measured directly from the scattering angle θ because $k_{||} = k_{in} \tan \theta \approx k_{in} \theta$ where k_{in} is the momentum of the incident electrons. The angle θ is usually less than 5° . The angular resolution is good, but the accuracy and resolution of the transmission method are limited by the necessity of using high energy electrons with the consequence that the mean free path of the incident electrons is of the same order of magnitude as, or greater than, the thickness of the film. The energy loss is of the order of a few electron volts and quite small compared to the 50 keV energy of the incident electrons. Furthermore, the sample has to be thin ($\sim 250 \text{ \AA}$) and is evaporated onto a substrate. The sample is a polycrystalline film so that the surface is not well characterized, and there is a problem of separating the surface effects from the substrate.

In the ILEED experiments the sample can be well characterized, and different orientations of a single crystal and adsorption of foreign atoms can be studied. However, the ILEED intensities are associated with elastic LEED resonances where multiple scattering precludes a simple theoretical analysis. To extract the SPDR from these data is, therefore, a very complicated procedure.

The Effect of Impurity Adsorption on Surface Plasmons

When the surface of a semi-infinite plasma is bounded by a dielectric layer of finite thickness τ , beyond which there is a vacuum, the surface plasmons have a dispersion relation (derived by Stern and Ferrell¹⁹):

$$\omega_s = \omega_p \left[\frac{\epsilon + \tanh k_{\parallel} \tau}{2\epsilon + (1 + \epsilon^2) \tanh k_{\parallel} \tau} \right]^{1/2} \quad (2)$$

In the limit $\tau \rightarrow \infty$, Eqn. (2) reduces to $\omega_p / \sqrt{1 + \epsilon}$. In the limit $\epsilon \rightarrow 1$ or $\tau \rightarrow 0$, Eqn. (2) reduces to $\omega_p / \sqrt{2}$. Murata and Ohtani²⁰ have used Eqn. (2) to determine the oxide thickness on aluminum by assuming a dielectric constant for the surface oxide. However, it is not clear whether the concept of dielectric constant is meaningful when the thickness is below some critical thickness, especially when the oxygen species is at submonolayer or monolayer coverage.

DESIGN AND OPERATING CHARACTERISTICS OF APPARATUS

Design Considerations

To minimize the effect of surface roughness due to the large sampling area at glancing incidence, the incident electron beam should be focused to very small diameter. For example, at $\theta_0 = 4^\circ$ the beam sampling area is 14 times the beam width. Hence, the design aims for ~ 0.1 mm beam width because the size of the sample is ~ 1.2 cm in diameter. Because the aim of this study is surface plasmon excitations, which have a large energy loss (~ 10 eV for aluminum), measured at off-specular directions, where the counting rate is expected to be low, the electron gun should produce reasonably high current, given the limitation of the small beam size, and, therefore, is not monochromatized. However, to lower the beam energy spread, an indirectly heated oxide cathode is operated at lower temperature ($\sim 1000^\circ\text{C}$) than a directly heated thoriated tungsten filament. The beam exhibits Maxwell energy distribution whose full width at half maximum (FWHM) is given by $\Delta E_K = 2.54 k_B T$. Thus the incident energy spread is ~ 0.22 eV. Additional energy spreads are possible, however, due to fringe fields.

Because of possible noise problems from rotating the Channeltron electron multiplier which is operated at ~ 3.5 kV and possible entanglement of many wires, the analyzer is fixed in position. The electron gun and the sample rotate about the vertical axis. To achieve energy resolution comparable to the cathode energy spread and to have a uniform angular resolution in our angular scattering experiment as well as high transmission efficiency, a hemispherical electrostatic energy analyzer, which possesses two-dimensional focusing, is used. Because of the space limitation, its mean radius is 2.54 cm.

To be sure that the axis of rotation of the sample and the electron gun

coincide and to facilitate alignment using lasers, the electron gun, the analyzer and the sample are mounted on the same Wheeler flange. In this arrangement they can be aligned outside the vacuum envelope and then lowered into the vacuum chamber. Figures 5 and 6 show respectively a photograph and a schematic diagram of the apparatus.

Vacuum System

The chamber is a stainless steel cylindrical ultrahigh vacuum chamber 30 cm in diameter and 47 liters of volume. The system is first pumped from atmospheric pressure down to $\sim 10\mu$ by means of two Varian Vacsorb zeolite cryogenic sorption pumps. At this pressure the titanium sublimation pump filaments are degassed and the 140 l/s Varian ion pump is turned on. When the pressure reaches $\sim 10^{-7}$ Torr, the pump is baked at $\sim 125^\circ\text{C}$ for several hours. When the pressure is $\sim 10^{-8}$ Torr, the system is baked with heating tapes at about 150°C for about 24 hours. During the bakeout the filaments of titanium sublimation pump and electron gun and ion bombardment gun as well as the sample and sample holder are outgassed. Thus the base pressure is $\sim 6 \times 10^{-10}$ Torr when the system is at room temperature after two days. When the cryopanel is filled with liquid nitrogen, the pressure reaches to $\sim 2 \times 10^{-10}$ Torr. However, the operating pressure is $\sim 1 \times 10^{-9}$ Torr about two to three hours after pumping out argon (from sample cleaning).

To study oxygen adsorption and to use argon for ion sputter-cleaning the sample, a manifold pumped by a Vacsorb pump and a small Varian 8 l/s ion pump was constructed. A Varian leak valve connects the manifold to the main chamber.

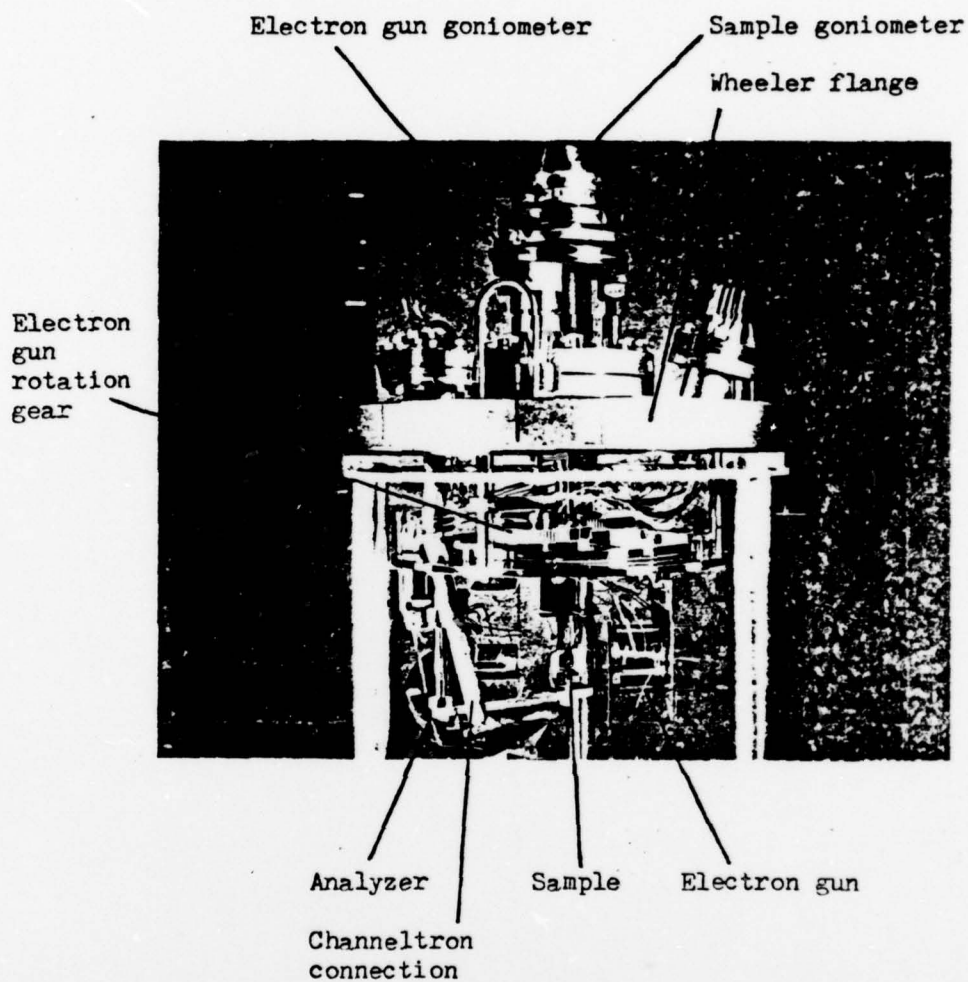


Fig. 5 A photograph of the apparatus.

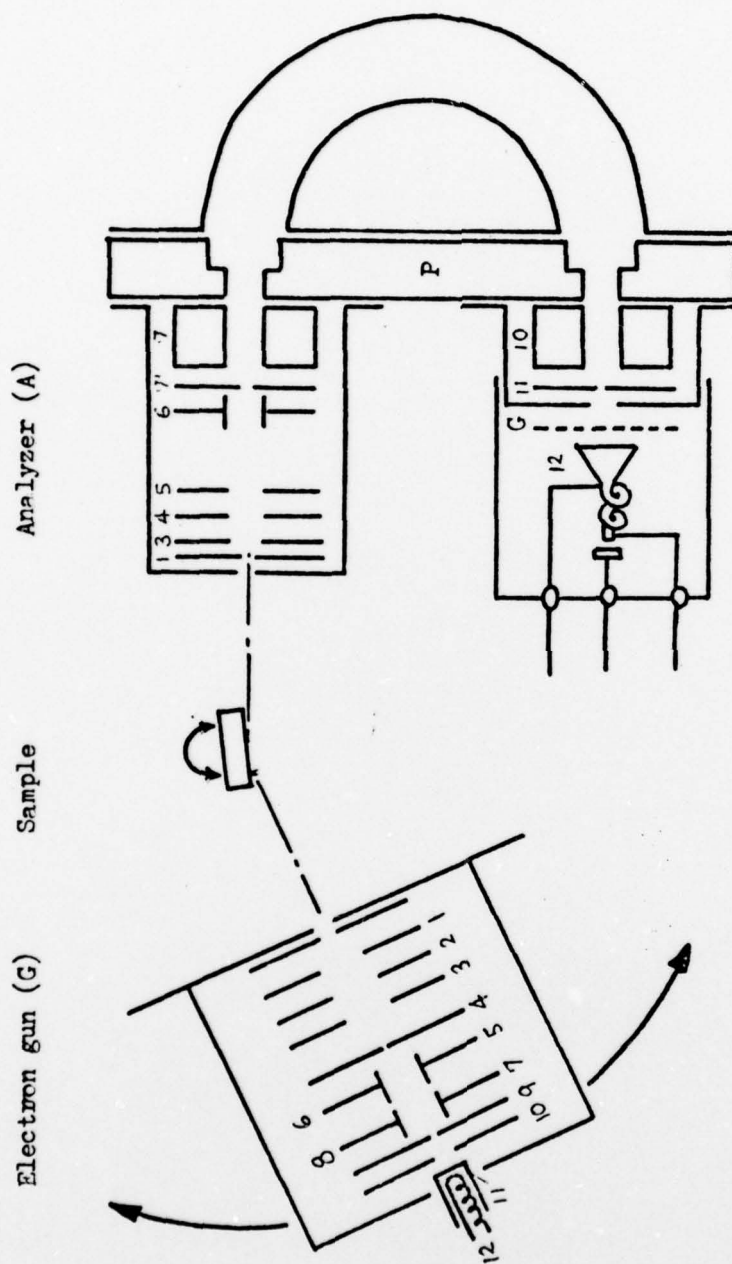


Fig. 6

A schematic diagram of the electron gun and the hemispherical energy analyzer. For the electron gun, G1-G3: zoom lens, G4: entrance pupil, G5-G8: deflectors, G9: anode, G10: "diode", G11: cathode, G12: heater. For the analyzer, A3-A5: zoom lens, A6: deflectors, A7'-P: tube lens, P: plate, P-A11: tube lens, G: grid, A12: Channel-tron electron multiplier.

Electron Gun

Figure 6 shows an inside view of the electron gun. Electrons are accelerated toward the grounded anode, passing through a "diode", which adjusts the emission current. The anode contains an aperture 0.63 mm in diameter which, together with G4 (0.13 mm aperture), collimates the beam. Inside this region there are two sets of deflector plates which are used to steer the beam, compensating any electron trajectory deviation due to fringing field or stray magnetic field.

After collimation, the electrons pass through a zoom lens, G1-G3, Fig. 6. The zoom lens operates in the Einzel mode, i.e., G3 is grounded, and G2 is the focusing electrode. For the gun $A = D = 3.8$ mm so that overall length of the gun is $\sim 4-5$ cm. When $V(G2) = 0.92 \times V(\text{cathode})$, the beam is focused on the sample with unit magnification at about 3.18 cm from G2. This is verified by testing the electron gun in a bell-jar and observing the beam spot on a ZnS screen positioned where the sample would be, with larger aperture G4 (1.3 mm). The beam size in this case is about 1 mm. The angle of divergence at the sample is calculated to be 0.5° , and the spherical aberration is small.

The electrodes are made of molybdenum to ensure uniform work function throughout the gun and to minimize the effects of surface potential of the electrodes. They are separated and insulated by 0.76 mm diameter sapphire balls.

Energy Analyzer

Figure 6 shows the construction of the hemispherical electrostatic energy analyzer which was first worked out by Purcell²¹. It is a modified

version of the Boness and Schulz analyzer²². The energy resolution is of course finite, depending on analyzing energy, instrument geometry, and operating conditions:

$$\Delta E/E_A \approx w/2R_0 + \alpha^2/2,$$

where w is the aperture diameter and α the angular divergence about the central ray of the entering beam.

There are two methods of operating the energy analyzer. One is sweeping the analyzing energy E_A , the other is analyzing at a constant energy E_A with pre-retardation. The advantage of the first method is its simplicity of operation and constant transmission, but the disadvantage is a varying energy resolution. The second method was adopted for its constant energy resolution over the entire spectral range.

Following Simpson²³ we employ a virtual aperture design, i.e., there are no physical apertures in the entrance and the exit planes. Instead, these planes are imaged by the electron lens onto physical apertures at much higher potential than exist in the spherical deflector. In this design the secondary electrons produced at the aperture are prevented from reaching the spherical deflector. Signal to noise ratio, therefore, is improved.

Because of the space limitation, the mean radius of the energy analyzer is set at 2.54 cm, and the overall length is about 7.6 cm. The inner and outer radii are chosen so that the maximum deviation from the central ray is $2/3$. This is calculated from the equation given by Kuyatt and Simpson²⁴ for the maximum deviation w_m of the beam in the spherical capacitor from the central ray of radius R_0 :

$$\frac{w_m}{R_o} = \frac{\Delta E}{E_o} + [\alpha^2 + (\frac{\omega}{2R_o} + \frac{\Delta E}{E_o})^2]^{1/2}.$$

Therefore, R_1 and R_2 are 1.90 cm and 3.18 cm respectively. The diameter of entrance and exit apertures, A7' and A11, are equal and such that $\Delta E/E_A \approx 3\%$. A smaller ratio can be obtained only at the expense of detection efficiency which could not be reduced in the present experiments where a minimum counting time is necessary to maintain a clean surface.

The incident energy ranges from 100 eV to 1 kV, and we want to analyze electrons at about 10 eV, with ΔE of 0.3 eV, comparable to the energy spread of the electrons from the indirectly heated cathode. An asymmetric three-aperture zoom lens focuses scattered electrons to the physical aperture A7'. Then the tube lens, consisting of A7 and P, focuses these electrons to the entrance plane of the hemispherical analyzer. After the electrons go through the energy dispersive deflector, they are focused from the exit plane to the physical aperture A11 by a similar tube lens, but operated in reverse. Then the electrons, after going through the grid for still further background reduction, are detected by the Channeltron electron multiplier.

Detection Electronics

The major electronic components for the analyzer have been described by Fraser *et al.*²⁵ Our operation is slightly different from theirs, as shown in Fig. 7. The retarding sweep voltage is reproducibly synchronized with the address advance of a 1024-channel Nicolet multichannel analyzer (MCA). Sweep control and data storage are provided by combining functions of the MCA and a "hard-wired" voltage programmer. All programming is done digitally and then converted to an analogue signal by a 15 bit digital-to-

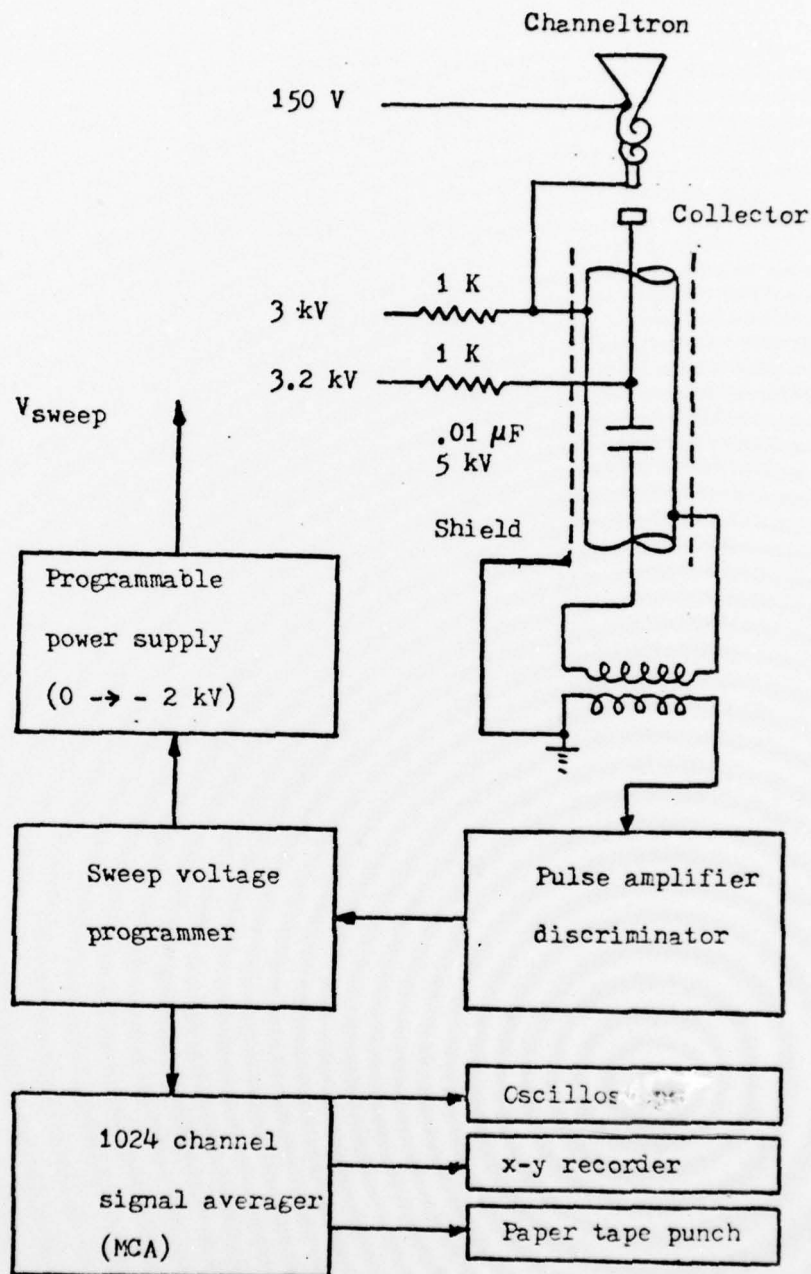


Fig. 7

Detection electronics.

analogue converter (Analog Devices). A modified Kepco high voltage operational power supply amplifies the output of the programmer to a maximum of -2.0 kV.

The Channeltron electron multiplier is used for its small size and high gain and is operated in the pulse mode. The pulse mode provides a great increase in sensitivity over analogue measurements and can also be made relatively insensitive to shifts in the gain of the electron multiplier which could occur during gas adsorption experiments. The output, typically negative pulses of amplitude 20 mV and 15 nsec width, is coupled by an isolation transformer (to eliminate the high DC level) to the input of a pulse amplifier discriminator designed to convert the signal to pulses of +5 V amplitude and 400 nsec duration. These output pulses are then stored in the memory of the MCA.

Pulse counting with repetitive retarding energy sweeps is used to increase the signal-to-noise ratio. For random events, the signal-to-noise ratio increases as \sqrt{N} , where N is the number of events. After a suitable time, usually when N for a surface plasmon peak is $\gtrsim 10^{+5}$ counts, one obtains a spectrum of electrons counted vs memory address (retarding voltage). This information can then be displayed on an oscilloscope, plotted on x-y point plotter, or punched on paper tape.

Sample Preparation and Cleaning

A high purity single crystal aluminum sample 1.27 cm in diameter and 0.32 cm thick was spark-cut and etched for about one minute in 70% phosphoric acid, 25% sulfuric acid and 5% nitric acid (by volume) at 68°C. Then, on the back side of the sample, a blind hole was spark-drilled and tapped for the mounting screw. The x-ray Laue pattern shows that the sample was cut

to about 1° of the (100) plane. Then the sample was polished by hand with 1μ and $1/4\mu$ diamond paste, and then electropolished in 90 ml distilled water, 525 ml ethanol, 25 ml 2-butoxyethanol, and 59 ml perchloric acid at 2.0 ± 0.2 Amperes current for 4 seconds.

Final cleaning was effected inside the chamber. When the sample was in vacuum ($\lesssim 10^{-9}$ Torr), the anodic oxide was removed in situ by an accumulated total of 48 hours of argon ion bombardment with ion energy 740 eV at current level of $0.5\mu\text{A}$ at the sample, followed by 12 hours of annealing at about 450°C . The cleanliness is monitored by surface plasmon energy and its dispersion. When the surface is dirty there is no surface plasmon peak, only a broad peak at 22 eV. When the surface is clean, the surface plasmon peak appears. Burkstrand²⁶ claimed that the most sensitive test of a change in the surface condition appears to be the reproducibility of the surface plasmon angular and loss profiles. Changes in the peak positions and intensities can be measured with about 0.02 and 0.03 monolayers coverage of background (mostly H_2) gases.

To be able to rotate the sample nearly 360° without the heating wires and thermocouple wires touching one another, we have constructed a sample holder as shown in Fig. 8 such that two #10 copper heater rods and the chromel-constantan thermocouple wires are fixed inside the central shaft. Resistive heating is achieved by conduction from the heated graphite support at the back of the sample.

Alignment

The sample is mounted and aligned to $\pm 2^\circ$, with the [110] close-packed direction in the (100) plane parallel to the incident electron beam. The tilt and translation screws of the sample goniometer are adjusted so that the shaft holding the sample wobbles within a circle of 0.010" diameter,

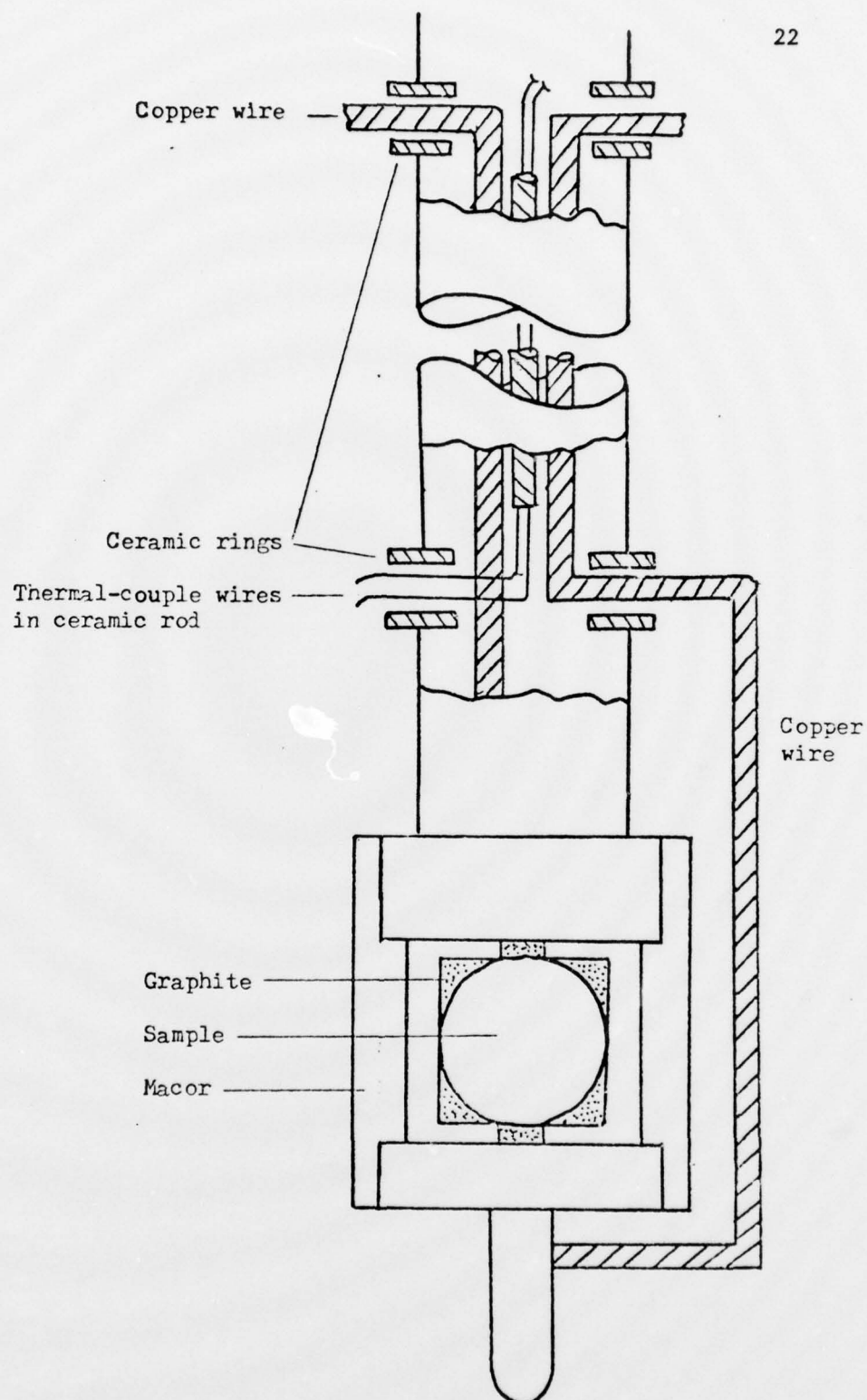


Fig. 8

A simplified schematic diagram of the sample holder. Macor is the machinable glass-ceramic.

measured with a dial gauge. Sample rotation angle of incidence is accurate to $1/2^\circ$ as measured by reflection of a laser beam.

Figure 9 shows the arrangement for the laser alignment. The outer hemisphere is first removed. The laser is aligned first perpendicular to the mounting plate of the analyzer so that the reflected laser beam from a glass side placed on the mounting plate (for the purpose of alignment) arrives at the laser aperture. Then the electron gun and the sample are rotated to intersect the transmitted laser beam. This defines θ° for θ_S and θ_G . Then the sample is rotated 45° , and the electron gun is rotated till its exit aperture intersects the reflected laser beam from the sample. This defines $\theta_G = 90^\circ$. When the whole apparatus is lowered into the vacuum chamber, the laser is first aligned perpendicular to the window, and then the whole apparatus is positioned so that at $\theta_S = 0^\circ$ when the reflected laser beam from the sample is reflected back to the laser aperture. See Fig. 9(c). Inside the vacuum chamber the electron gun rotation is determined by

$$\theta_G = 90^\circ - 2 |\theta_S|.$$

However, this is only approximate since the laser beam may not be reflecting from the center of the sample, indicating an incorrect θ_G . Therefore, the specular direction is determined by rotating the sample until a maximum appears in the intensity of the elastic peak. The overall angular accuracy is estimated to be $\pm 1^\circ$.

Energy Resolution

Figure 10(a) shows the current at the first aperture of the analyzer as a function of the electron gun deflector setting. It shows that the electron beam is aligned with the analyzer when there is no deflection

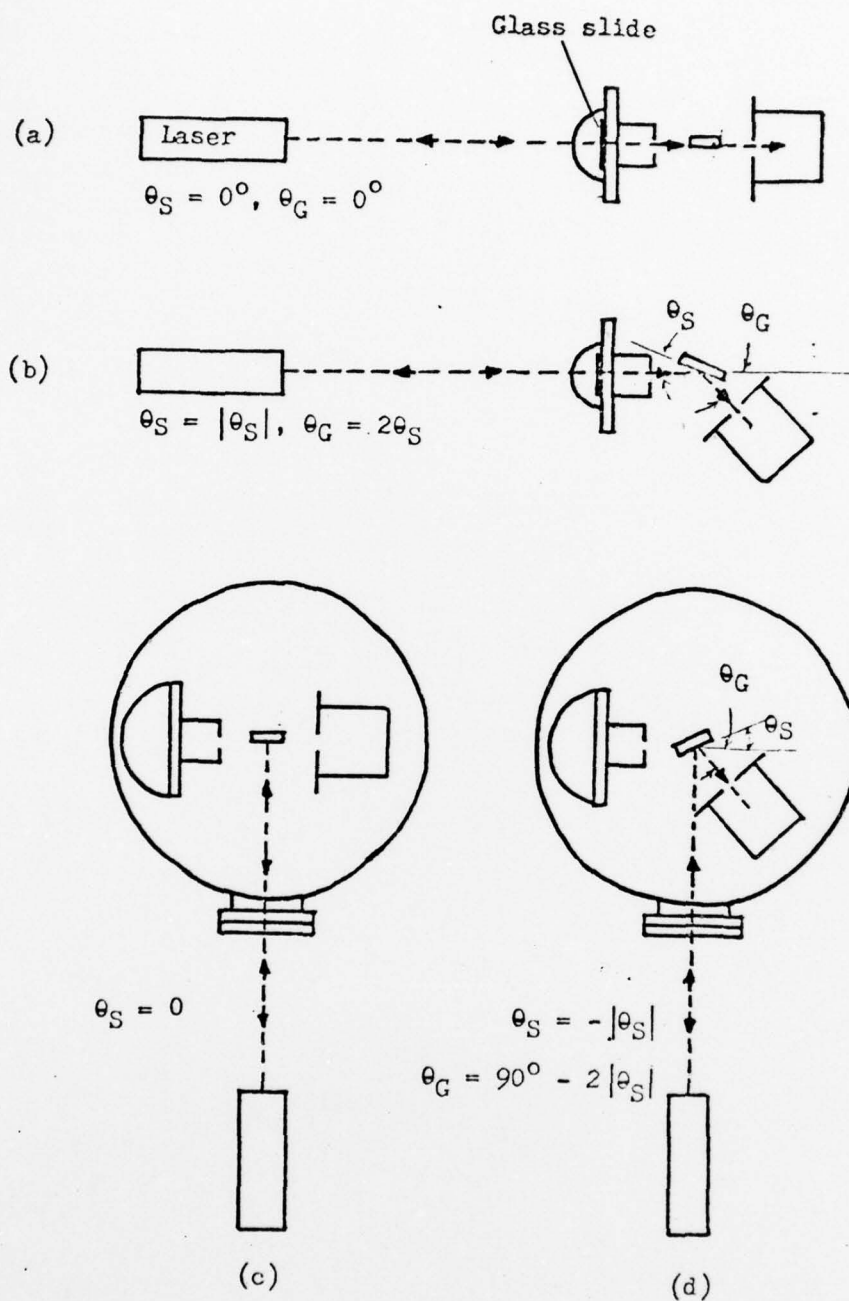


Fig. 9

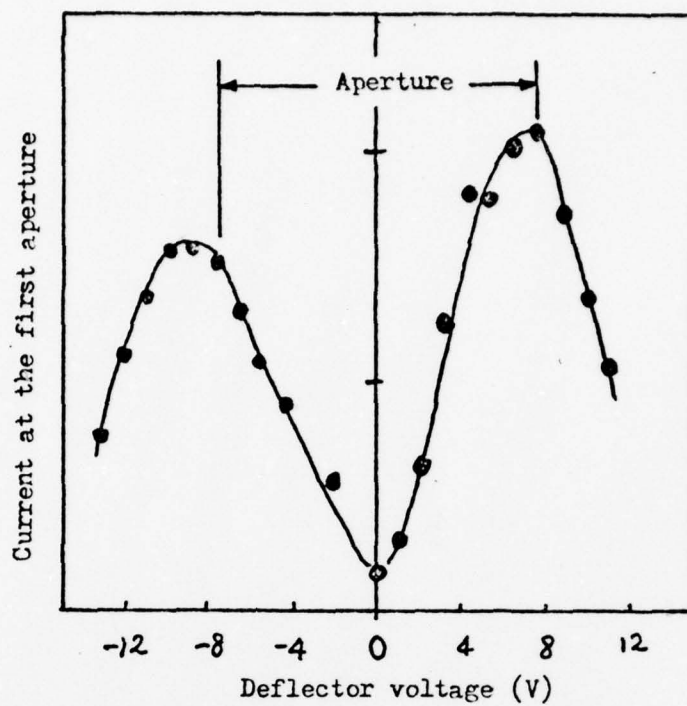
Alignment procedures. See the text for an explanation.

voltage applied. Hence, the magnetic field (compensated with Helmholtz coils) is not a problem for the incident electrons since the Larmor radius of a 500 eV electron in the residual field of 20 mG is about 4000 cm. Figure 10(b) shows a spectrum of the main beam. The incident energy is 500 eV, and the FWHM is 0.36 eV. This is consistent with adding in quadrature the energy spread of the incident electron (0.22 eV) and the energy resolution of the analyzer (0.3 eV).

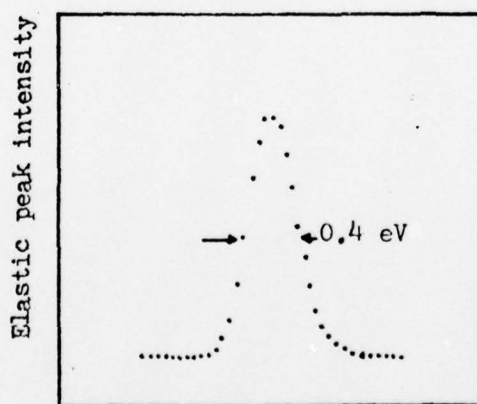
Angular Resolution

Figure 11(a) shows the angular resolution taken at $\theta_0 = 4^\circ$. The FWHM is about 3.5° . There is a slight asymmetry due to the large illuminated area on the sample, i.e., some scattered electrons are closer to the analyzer than others. This angular resolution is used in the oxygen experiments.

However, for the SPDR determination better angular resolution (hence better wave vector resolution) is needed. To achieve this, electrodes A4 through A6 are grounded, effectively using the aperture A7' as the defining aperture. A typical result is shown in Fig. 11(b). The FWHM is slightly less than 1.5° .



(a)



(b)

Fig. 10 (a) Current at the first aperture of the analyzer as a function of the deflector voltage.

(b) The elastic peak profile.

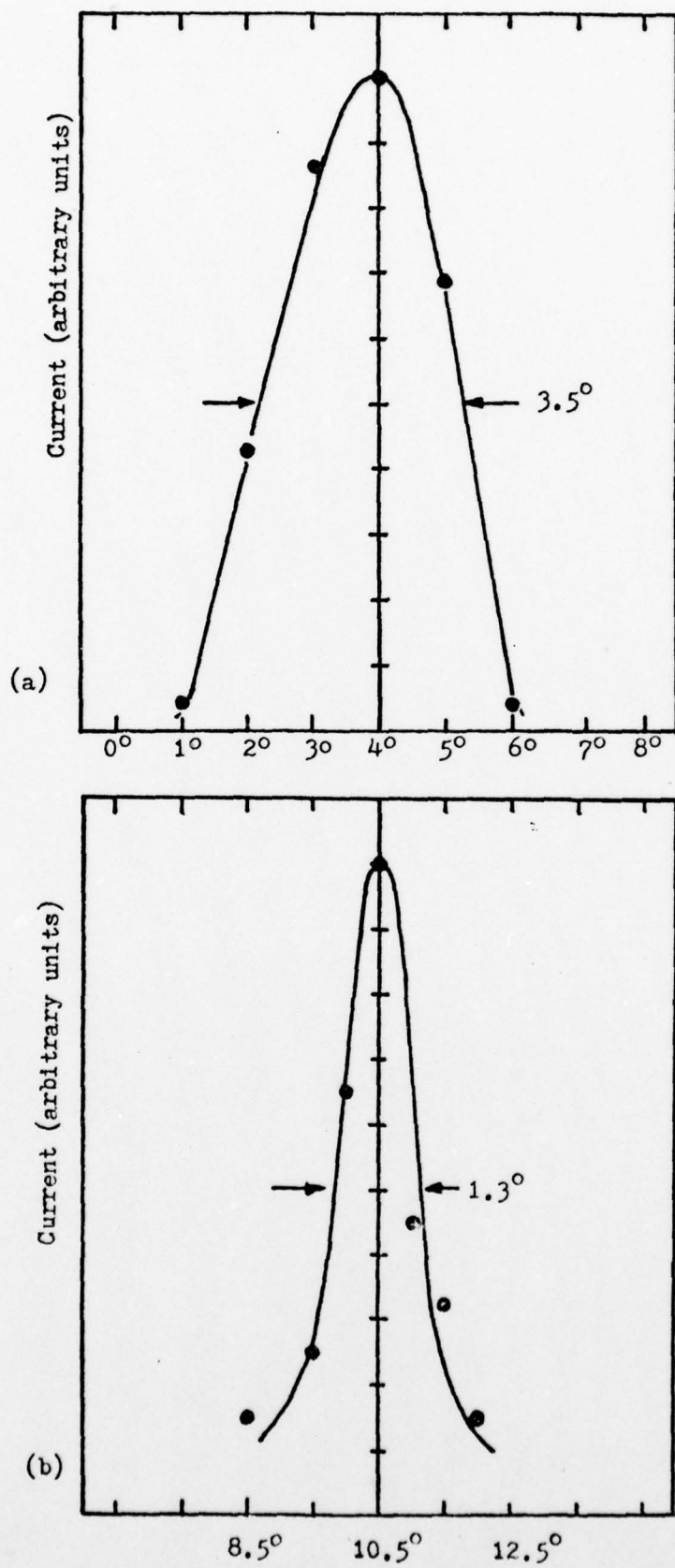


Fig. 11 Angular resolution of the spectrometer.

EXPERIMENTAL PROCEDURE

Glancing Incidence

In our experiment the electrons are directed at a glancing angle to the surface to exclude complications due to multiple scattering from the bulk. The mean free path of an electron with energy between 40 eV and 600 eV in aluminum is $\sim 10 \text{ \AA}$ ¹ so that at glancing incidence (10° to the surface) the penetration depth is $\sim 1.7 \text{ \AA}$ ^o. Consequently, only the first and, at most, the second layers of atoms at the surface participate in the scattering process. In our experiment, then, only incident angles $\leq 10^\circ$ are employed.

We use 500 eV incident energy for two reasons. First, the energy cannot be too low because of the large polarization effect at glancing incidence for low energy electrons. The polarization effect comes from the image potential induced by incoming electrons near the metallic surface, causing the electron trajectory to be modified. Feinstein²⁷ estimated that when the electron energy is very much larger than 100 eV, the effect of polarization on the grazing electron trajectory is small. At the same time, while the energy has to be as high as possible because we are interested in high momentum surface plasmons and the momentum varies as the square root of energy, the energy must also be low enough so that the mean free path is short. Consequently, 500 eV is chosen as an optimum experimental condition.

Because the multiple-scattering dynamic effect is small at glancing incidence, we shall apply the conservation law model to extract the SPDR.

$$E_o = E' + \hbar\omega_{sp}$$

(3)

$$k_o \cos \theta_o = k' \cos \theta' + k_{||}$$

where θ_o and θ' are measured from the surface, Fig. 2.

$$\begin{aligned} k_{||} &\approx k_o (\cos \theta_o - \cos \theta') \\ &\approx k_o \left(\frac{\theta_o^2}{2} - \frac{\theta'^2}{2} \right) \\ &\approx k_o (\theta_o - \theta') \frac{(\theta_o + \theta')}{2} \end{aligned}$$

Momentum Determination

There is a small correlation to $k_{||}$ as calculated from Eqn. (3) due to the finite acceptance angle of the analyzer. (This correction has not been noted by previous authors.) For an electron detected within the cone of angular acceptance, but outside the plane of incidence as defined by the incoming direction and the normal to the surface, the wave vector has a transverse component to the incident direction as shown in Fig. 12.

$$\begin{aligned} k_{||} &= [(k_o \cos \theta_o - k' \cos \theta \cos \phi)^2 + (k' \cos \theta \sin \phi)^2]^{1/2} \\ &\approx [(k_o \cos \theta_o - k' \cos \theta)^2 + k_o k' \cos \theta_o \cos \theta \cdot \phi^2]^{1/2} \end{aligned} \quad (4)$$

where ϕ is small, $\lesssim 1^\circ$.

Hence, we see that $k_{||}$ averaged over the analyzer acceptance is larger than the $k_{||}$ calculated from Eqn. (3). To estimate the magnitude of this increment, consider the case of large $k_{||}$ and small θ_o, θ' . From Eqn. (4)

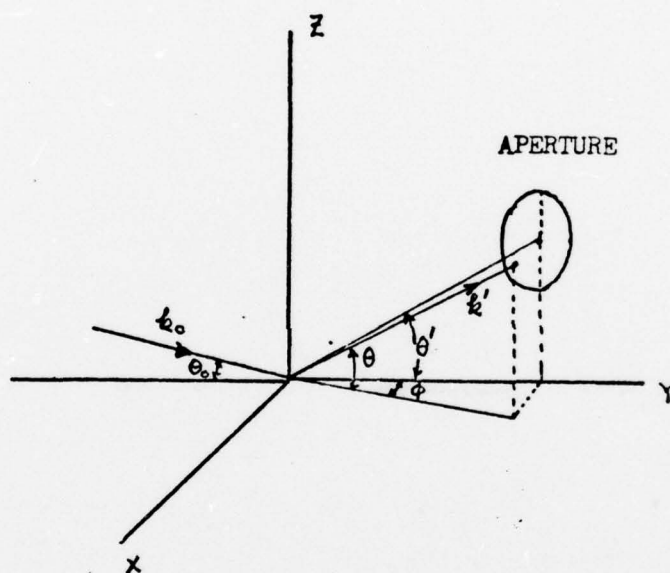


Fig. 12

The geometry for calculating the surface plasmon momentum.

$$k_{\parallel} \sim (k_{\parallel 0} + k_o^2 \phi^2)^{1/2}$$

$$\sim k_{\parallel 0} + \frac{1}{2} \frac{k_o^2 \phi^2}{k_{\parallel 0}} \quad k_{\parallel 0} \gg k_o \phi$$

Then

$$\langle k_{\parallel} \rangle = k_{\parallel 0} + \frac{1}{2} \frac{k_o^2 \langle \phi^2 \rangle}{k_{\parallel 0}} \quad k_{\parallel 0} + \Delta \langle k_{\parallel} \rangle$$

Taking $\langle \phi \rangle$ to be the standard deviation of the acceptance angle and $k_o = 12 \text{ \AA}^{-1}$, and $k_{\parallel 0} = 0.4 \text{ \AA}^{-1}$, we have $\Delta \langle k_{\parallel} \rangle \sim 0.02 \text{ \AA}^{-1}$. We expect that this correction is smaller at high k_{\parallel} than at small k_{\parallel} ($\sim 0.12 \text{ \AA}^{-1}$).

If we assume the angular acceptance to be a Gaussian distribution in θ and ϕ with the same standard deviation:

$$G(\phi, \theta', \sigma) = \frac{1}{\sqrt{2\pi}\sigma} e^{-(\theta - \theta')^2 / \sigma^2}$$

$$G(\phi, 0, \sigma) = \frac{1}{\sqrt{2\pi}\sigma} e^{-\phi^2 / \sigma^2}$$

Then we can calculate the averaged wave vector of the electrons detected and its standard deviation:

$$\langle k_{\parallel} \rangle = \int_{-\infty}^{+\infty} \int_{-\infty}^{+\infty} d\theta d\phi k_{\parallel} G(\theta, \theta', \sigma) G(\phi, 0, \sigma) \quad (5)$$

An implicit assumption is that the scattered electrons illuminate the aperture uniformly. Because angular acceptance is peaked in the ideal direction of the analyzer ($\theta = \theta'$, $\phi = 0$), the integration limit can be from $-\infty$ to $+\infty$. The standard deviation of $\langle k_{\parallel} \rangle$ is

$$\sigma_{k_{\parallel}}^2 = \langle k_{\parallel}^2 \rangle - \langle k_{\parallel} \rangle^2 \quad (6)$$

The $\langle k_{\parallel}^2 \rangle$ term can be integrated analytically, and $\langle k_{\parallel} \rangle$ is calculated using numerical integration.

The result indicates that for an acceptance angle of $\sim 1.5^\circ$, $\Delta \langle k_{\parallel} \rangle$ is about 0.02 to 0.04 \AA^{-1} in our energy and angular range, and $\sigma_{k_{\parallel}}$ is between 0.03 to 0.04 \AA^{-1} .

EXPERIMENTAL RESULTS

Energy Loss Spectra

An energy loss spectrum of the clean sample at specular reflection and different incident angles is shown in Fig. 13, where three spectra, taken with an incident energy of 500 eV and at incident angles, θ_o , of 38° , 22° , and 10° are compared. As expected, at high angle of incidence ($\theta_o = 38^\circ$) the volume plasmon dominates, and there are losses due to a volume plasmon and a surface plasmon, and two volume plasmons. At $\theta_o = 22^\circ$, surface plasmons are dominant but volume plasmons are still present. At glancing incidence ($\theta_o = 10^\circ$), volume plasmons have completely disappeared and only surface plasmons and their multiples are present. Furthermore, the ratio of the intensity of surface plasmon to that of the elastic peak increases with glancing incidence, as $1/\sin\theta_o$.

Figures 14 to 17 show energy loss spectra which exhibit the dispersion of surface plasmons. These spectra are obtained in two steps. First, a wide range of energy loss, encompassing both elastic and surface plasmon peaks, is scanned a number of times. Second, when the position of the elastic peak is determined, a narrow range of energy loss between 8.5 eV and 12.5 eV, covering only the surface plasmon energy, is scanned many times. Because of the arrangement of the electron gun, the sample and the analyzer, it is easier to fix the scattering angle, $\theta_o + \theta'$, then rotate the sample, thereby changing θ' and θ_o simultaneously. The loss spectra are correspondingly labelled by (θ_o, θ') . Also shown are values of $k_{||}$ computed from Eqn. (5).

In the $(4^\circ, 16^\circ)$ loss spectra in Fig. 14, the surface plasmon has an energy 10.4 eV, much lower than expected, even though its wave vector

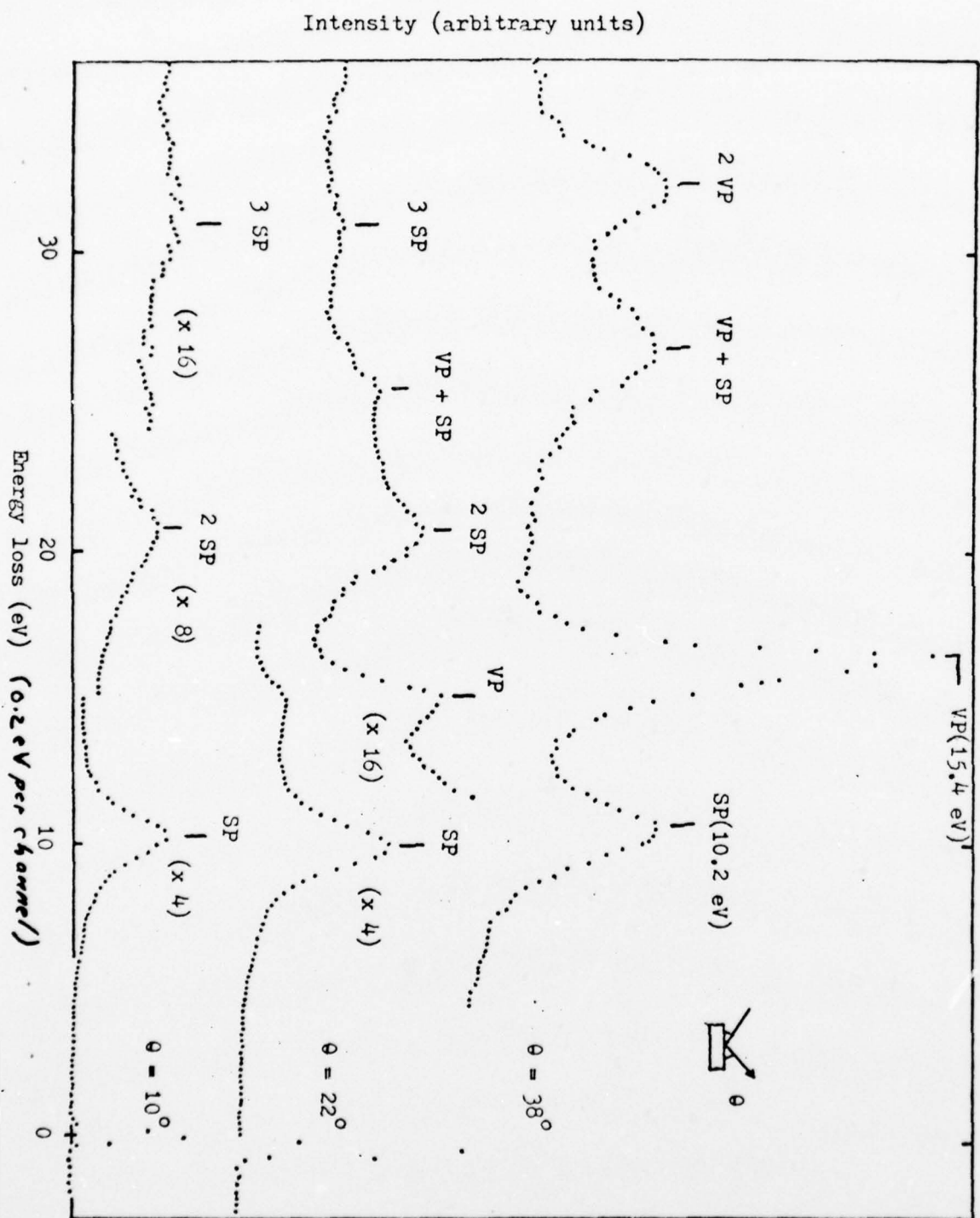


Figure 13

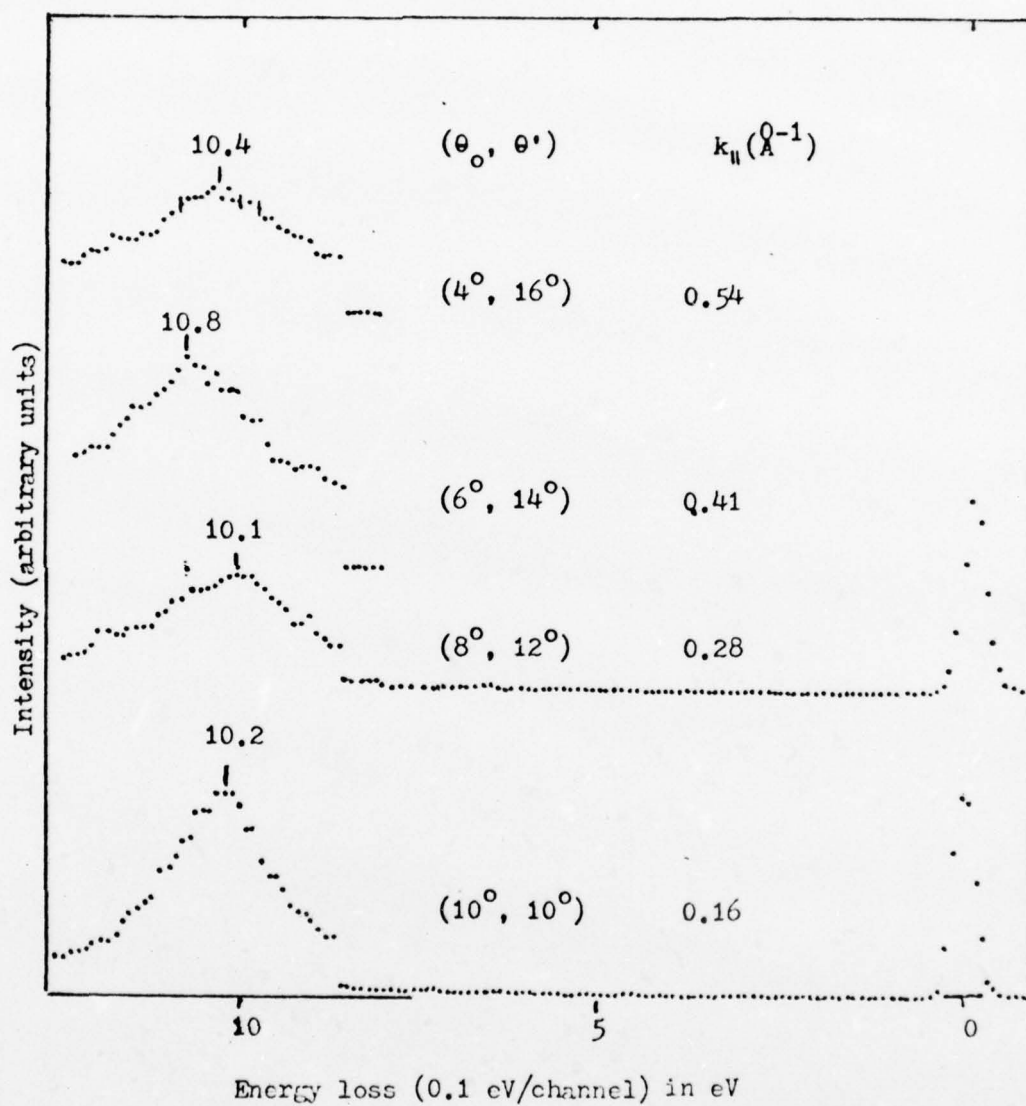


Fig. 14

Energy loss spectra for $\theta_0 + \theta' = 20^\circ$. Three typical statistical errors are shown as dashes on the top spectrum. The energy loss scale is 0.1 eV

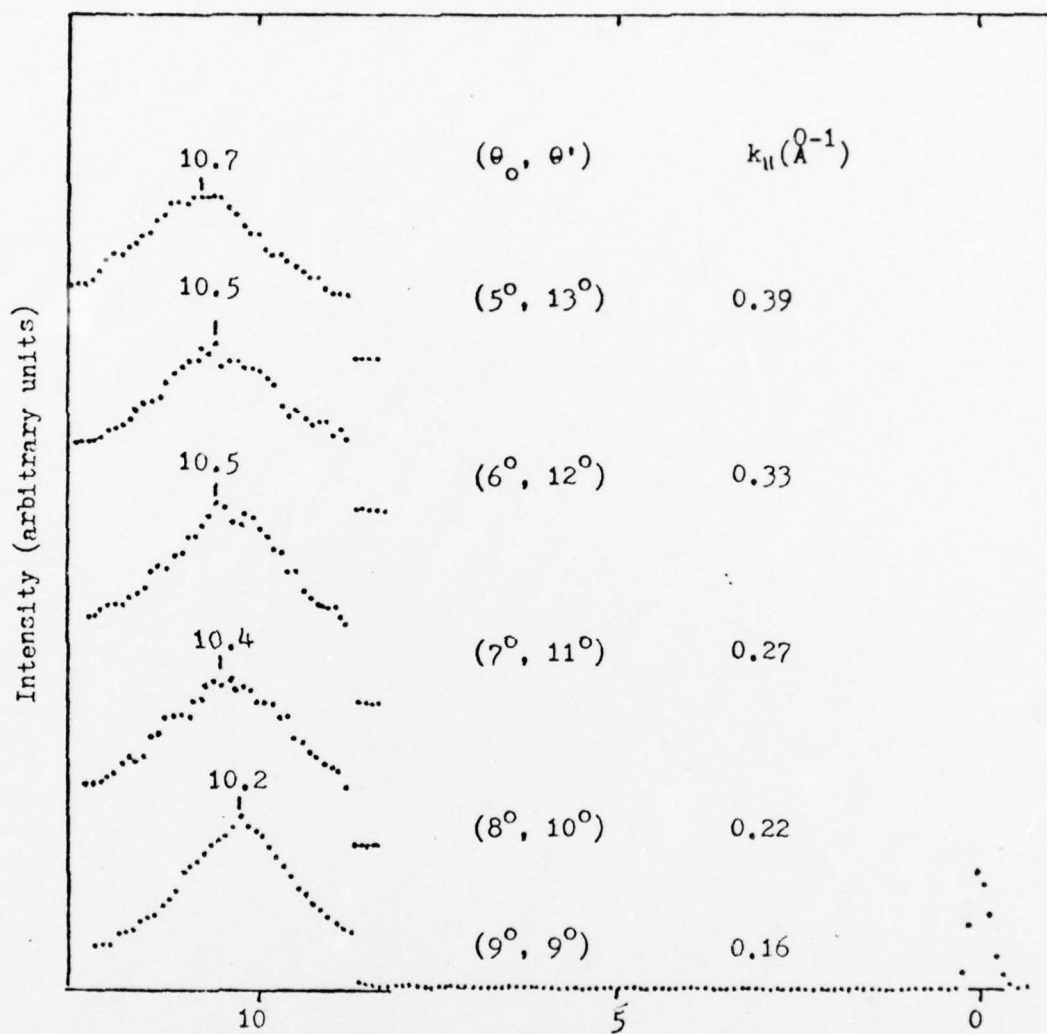


Fig. 15

Energy loss spectra for $\theta_0 + \theta' = 18^\circ$. Energy loss scale is 0.1 eV per channel.

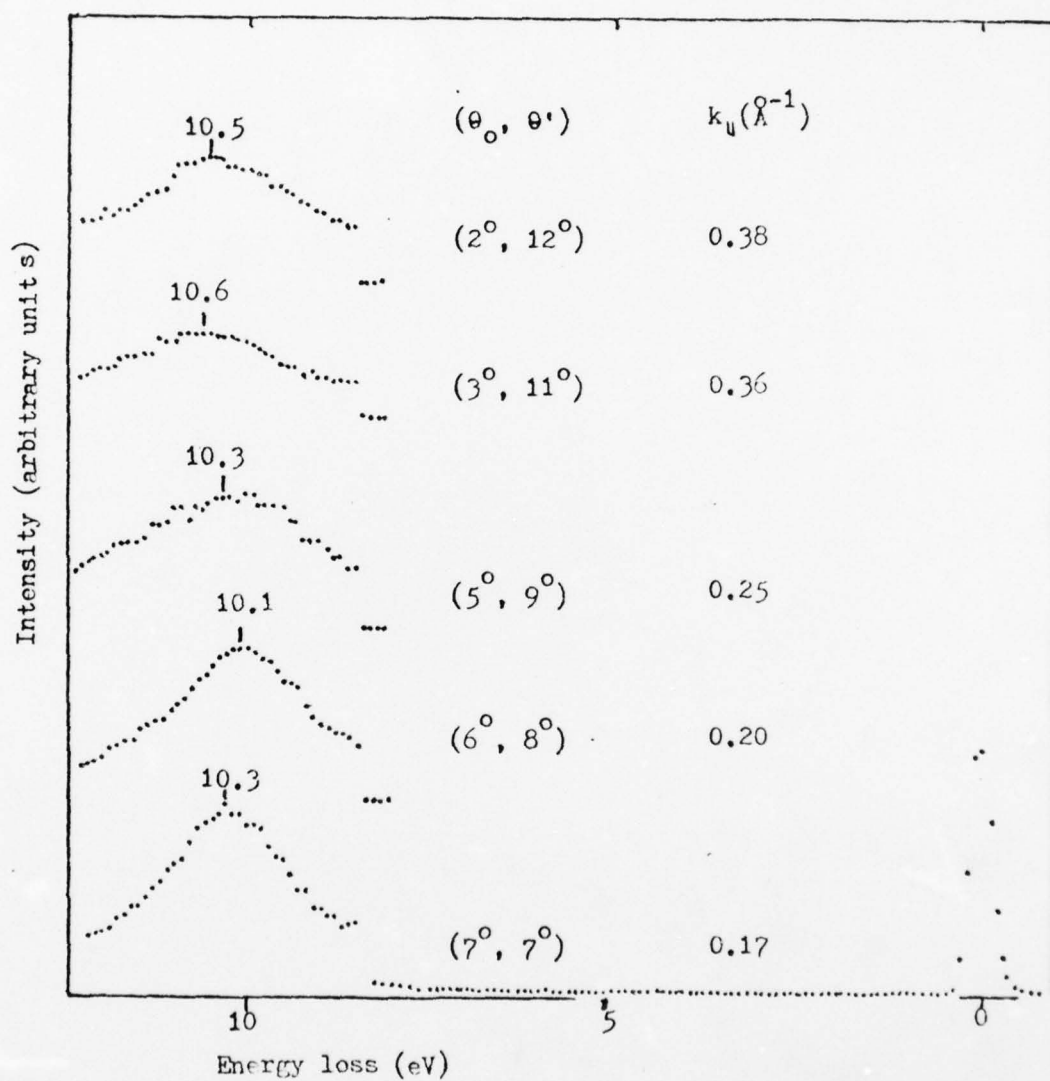


Fig. 16

Energy loss spectra for $\theta + \theta' = 14^\circ$. Energy loss scale is 0.1 eV per channel.

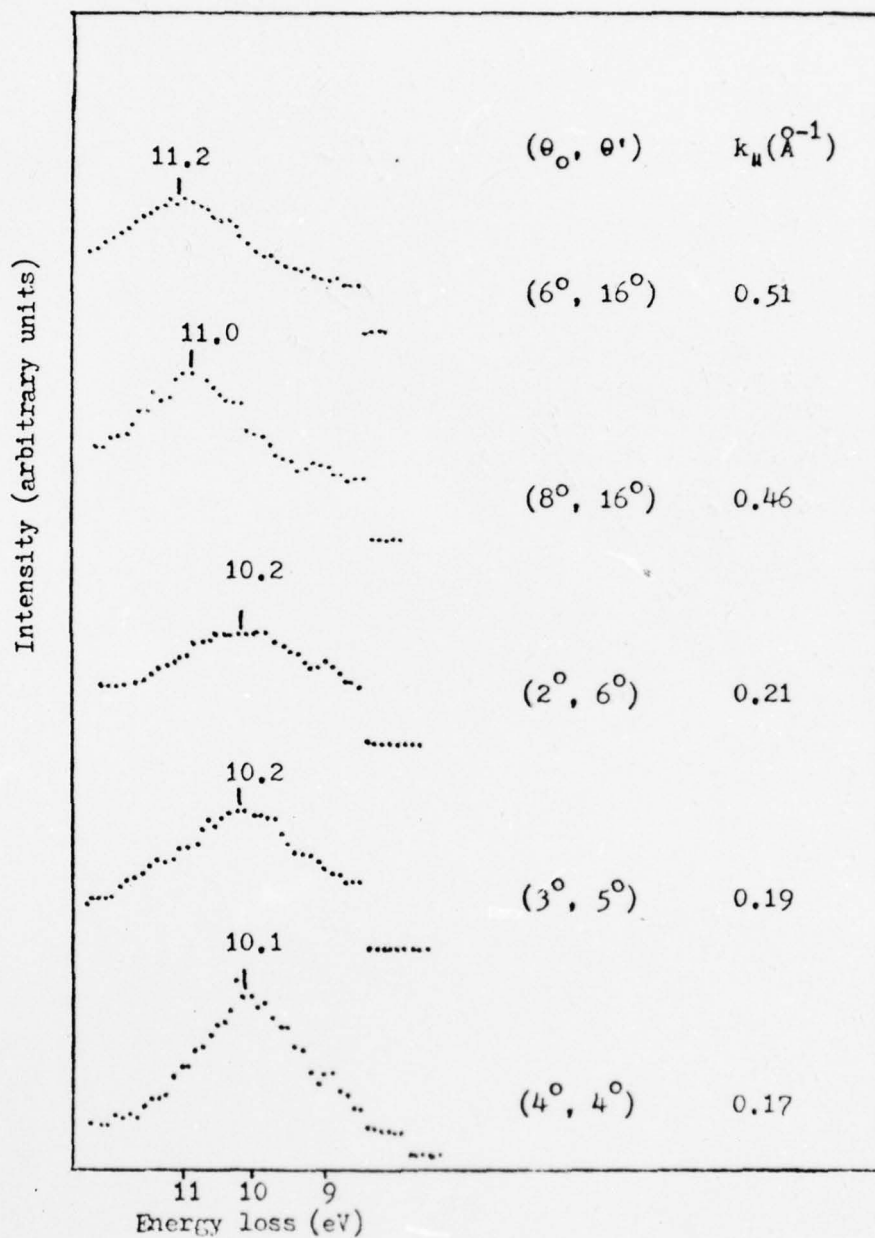


Fig. 17

Energy loss spectra. Energy loss scale is 0.1 eV per channel.

is calculated to be 0.55 \AA^{-1} . This is probably due to the effect of incoherent inelastic scattering, where incident electrons undergo nonspecular elastic scattering and inelastic scattering, creating a surface plasmon with lower k_{\parallel} . A similar situation occurs to a lesser extent for the $(2^{\circ}, 12^{\circ})$ loss spectra in Fig. 16.

It is difficult to determine the damping parameter for surface plasmons, because the FWHM of the surface plasmon peak is also influenced by the incident angles. At $\theta_0 = 2^{\circ}$ and 3° , the surface plasmon peaks appear broader than those with the same k_{\parallel} but higher θ_0 . (See Figs. 15 to 17). This indicates that the incoherent inelastic background is larger at these extreme glancing angles, possibly due to surface roughness.

Comparison with Spectra Obtained from ILEED

Figure 18 shows the SPDR as determined from the peak position and calculated k_{\parallel} in the loss spectra.* The two spectra with $(4^{\circ}, 16^{\circ})$ and $(2^{\circ}, 12^{\circ})$ are omitted. The horizontal error bar in each data point, calculated from Eqn. (6), reflects the finite acceptance angle, and the vertical error bar is essentially limited by the 0.1 eV per channel in the experiment. A least-square curve fitting is applied to these data points, in addition to which we require—following Duke *et al.*²⁸—that at $k_{\parallel} = 0$, $\hbar\omega_{sp} = 10.4 \text{ eV}$. This is to be consistent with data from high energy electron transmission through thin polycrystalline aluminum film²⁹ (where small k_{\parallel} can be probed) and with data from ILEED on epitaxial Al(111) film³⁰ (see Fig. 19) because the surface plasmon energy should be

* The peak position is determined by an eye-ball fit of a smooth curve through the loss spectra. A curve fitting with a Lorentzian, after appropriate background subtraction, will be performed later. The general trend of the SPDR and the discussion in the following section will not be affected.

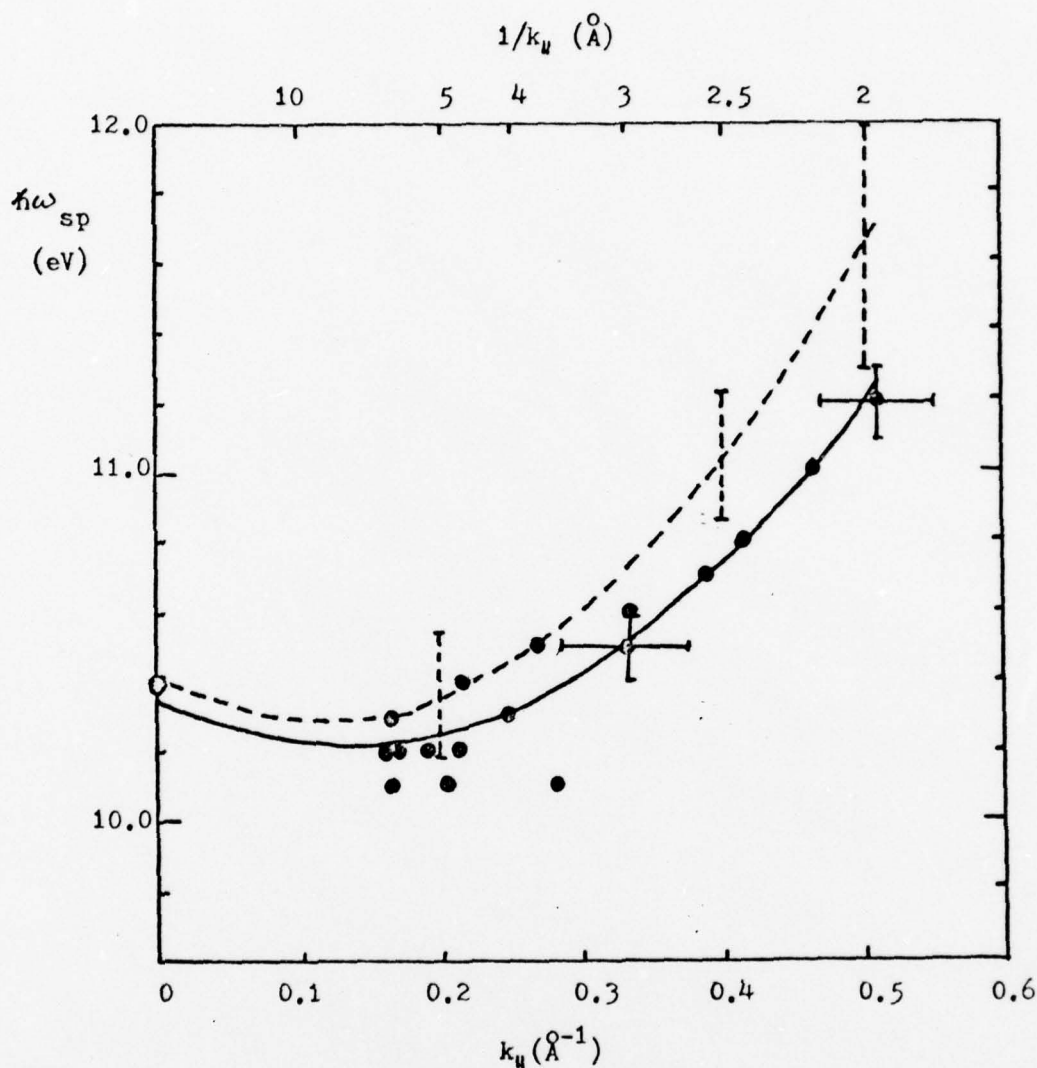


Fig. 18

The surface plasmon dispersion relation for Al(100) extracted from the energy loss profiles. The solid dots are the data points, and the solid line is the least-square fit through these points. The dashed line is the best fit obtained by Duke *et al.*:²⁸ ILEED (inelastic low energy electron diffraction) data. The open circle at $k_{||} = 0$ and $\hbar\omega_{sp} = 10.4$ eV is used in both fits to be consistent with ω_{sp} data from high energy electron transmission through polycrystalline Al and ILEED data for Al(111) because $\hbar\omega_{sp}$ should be independent of electron density profile at $k_{||} = 0$. The top horizontal scale is $1/k_{||}$ in \AA , the decay length of surface plasmon field into the bulk and into the vacuum.

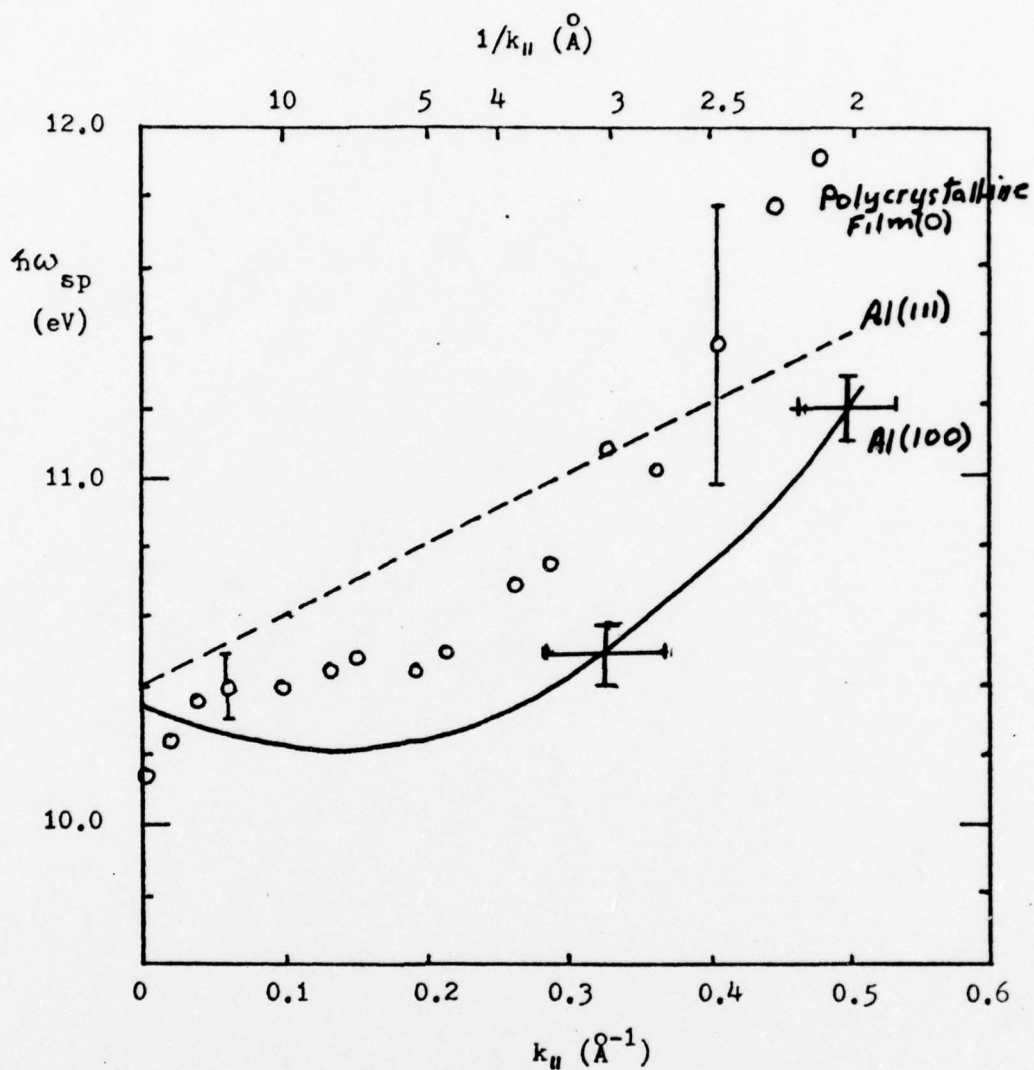


Fig. 19.

Surface plasmon dispersion relation for different faces of aluminum. The solid line is our best fit for Al(100). The dashed line is the best fit of Duke and Landman⁵ for the ILEED data of epitaxial Al(111) film of Porteus and Faith⁴. The open circles are some of Krane and Raether's data points from high energy electron transmission through thin polycrystalline aluminum film.¹⁰

independent of the electron density profile at the surface at $k_{\parallel} = 0$.

The resulting fit is

$$\hbar\omega_{sp} = 10.34(\pm 0.08) - 1.9(\pm 0.6)k_{\parallel} + 7(\pm 1)k_{\parallel}^2$$

where energy is in eV and momentum (or wave vector) is in \AA^{-1} . Also shown in Fig. 18 is a most recent best fit by Duke *et al.*²⁸ for ILEED data on Al(100) by Porteus and Faith³¹ and Wendelken³²:

$$\hbar\omega_{sp} = 10.4 (\pm 0.1) - 2(\pm 1)k_{\parallel} = 9(\pm 3)k_{\parallel}^2$$

The error estimates are performed in a complementary sense, i.e., decreasing A_1 , the linear coefficient, is accompanied by increasing A_2 , the quadratic coefficient, and vice versa. Our data is in general below Duke *et al.*'s best fit but, within the error estimates of both curves, the agreement is reasonably good.

Figure 19 shows SPDR's for different faces of aluminum. The solid line is our best fit for Al(100). The dashed line is the best fit of Duke and Landman³⁰ for the ILEED data of epitaxial Al(111) film of Porteus and Faith³³. The open circles are some of Krane and Raether's data points from high energy electron transmission through thin polycrystalline aluminum film²⁹. We see that SPDR's for different faces of aluminum and for polycrystalline aluminum are qualitatively different.

COMPARISON WITH THEORETICAL DISPERSION RELATIONSHIPS

Many theoretical models of surface plasmons have been constructed following two major approaches: quantum-mechanical or semi-classical microscopic RPA, and classical hydrodynamics. Feibelman develops a microscopic RPA with a step-function static density profile³⁴. The real co-

efficient of the linear term, A_1 , is found to vanish and it is proved that $\omega_s \rightarrow \omega_{so}$ and $k_{||} \rightarrow 0$ independent of the structure of the surface. He uses a time Fourier transform of Laplace's equation, a procedure which has been criticized by Newns³⁵, who points out that its validity is strictly confined to density variations of wavelength greater than that of the plasmon excitation. Newns concludes, using a time-dependent Hartree approximation applied to an infinite square barrier model that $A_1 \neq 0$. This conclusion is also supported by Beck³⁶ and by Heger and Wagner³⁷, using a full quantum mechanical RPA. Beck and Celli³⁸ have attempted a more realistic RPA calculation by introducing the surface as a step-function potential barrier. Their calculations are performed with the aid of a new variational principle. Although it is claimed that no adjustable parameters are involved, they do introduce variational parameters, and a good choice of trial function seems to be quite important. Their result shows that $A_1 < 0$.

Figure 20 compares the experimental curve with the above-mentioned calculations as well as two hydrodynamic infinite-barrier-model calculations^{39,40}, where both the linear and quadratic terms are presented. We see that the agreement is not very good. The infinite-barrier models all require a too rapid dispersion.

This result is to be expected from the following considerations. Since the field associated with surface plasmons penetrates into the bulk with a decay length of $1/k_{||}$, at high $k_{||}$ the surface plasmon field penetrates less into the bulk so that the average charge density involved in the surface plasma oscillation decreases and so does the effective $\omega_p / \sqrt{2}$. Therefore, the gradual decrease of the charge density at the surface has the effect of lowering the plasma frequency with increasing $k_{||}$. In the

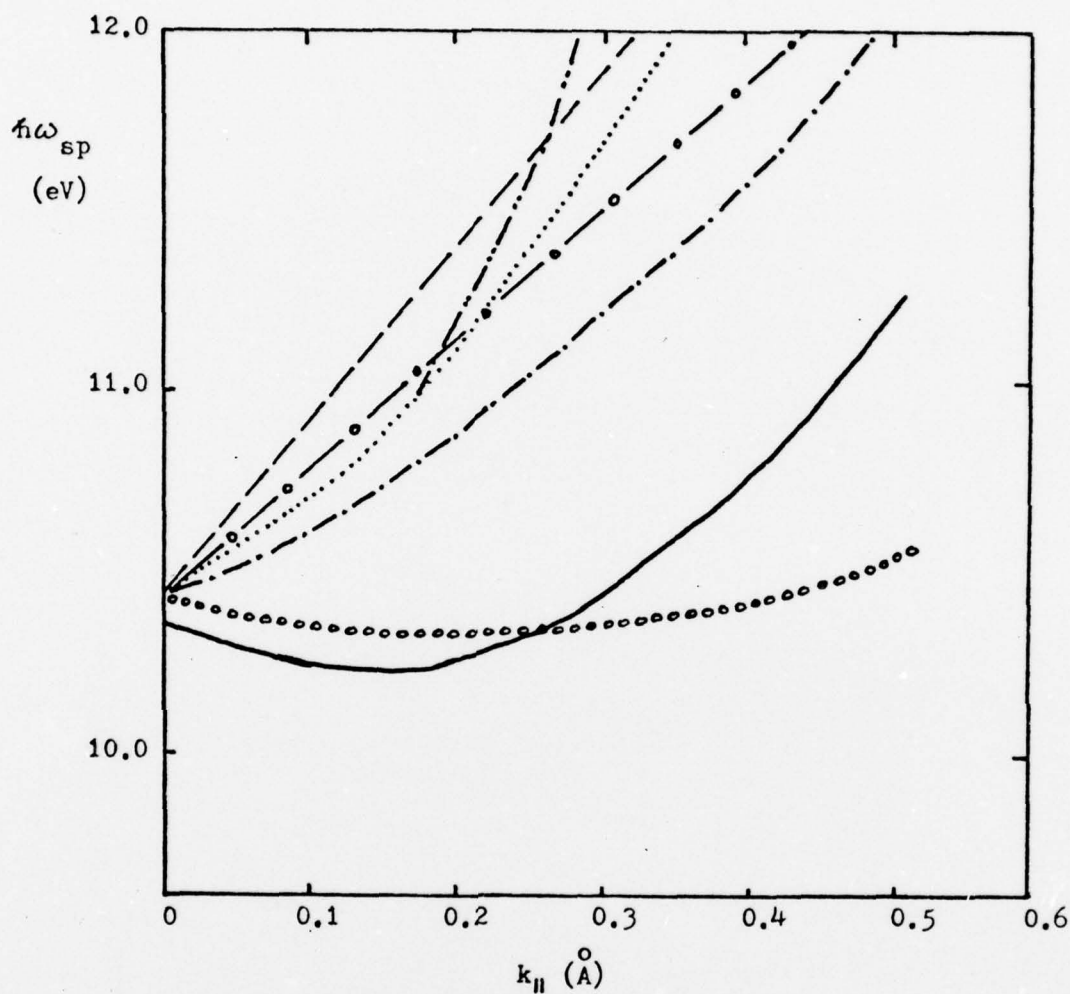


Fig. 20.

Comparison of the least-square fit of the surface plasmon dispersion relation (SPDR) of Al(100) (—) with some theoretical calculations of the SPDR.

Infinite-barrier hydrodynamic models:

— — — Ritchie⁴¹

- · - · - Ritchie and Marusak³⁹

..... Heinrichs⁴⁰

Infinite-barrier random-phase-approximation models:

- · - · Beck³⁶

- · - · Heger and Wagner³⁷

Step-function random-phase-approximation model:

· · · · Beck and Celli³⁸

language of the hydrodynamic model, the internal pressure of the electron gas, or the resistance against compression, increases the plasma frequency with increasing k_{\parallel} . Hence, the combined result is a plateau region and a slower rise, as compared to the infinite-barrier models, which are not affected by the decrease in electron density at the surface.

It is worthwhile at this point to consider in more detail a general relation derived by Harris and Griffin⁴² for the linear coefficient A_1 . They describe the dynamics of an inhomogeneous system in terms of the Wigner distribution function $f(\vec{P}, \vec{r})$ which is essentially the excess density of particles with momentum $\hbar\vec{P}$, at point \vec{r} , due to the action of the total one-electron potential. In the high frequency approximation, i.e., to leading order in k_{\parallel}/ω , they obtain

$$A_1 = \frac{1}{2} \lim_{k_{\parallel} \rightarrow 0} \frac{\int_{-\infty}^{\infty} dz z \delta n(z)}{\int_{-\infty}^{\infty} dz \delta n(z)} + \int_{-\infty}^{\infty} dz \rho(z) \quad (7)$$

where $\delta n(z)$ is the fluctuating charge density associated with surface plasmons. The static density profile, $n_0(z)$, has been split into two parts

$$n_0(z) = \bar{n}(\theta(z) + \rho(z))$$

where $\rho(z)$ is the static deviation from a step-function $\theta(z)$. The second term on the right hand side of Eqn. (6) vanishes as a result of charge neutrality. It is always possible to choose the origin of z such that this term vanishes. The first term is clearly related to the charge dipole associated with the density fluctuation of surface plasmons.

To calculate A_1 one needs to know $\delta n(z)$ or its Fourier component $\delta n(k_{\parallel}, k_z, \omega)$ which, in the high frequency approximation, equals⁴²

$$\delta n(k_{\parallel}, k_z, \omega) = \frac{4\pi e^2}{m\omega^2} \int_{-\infty}^{\infty} \frac{dP_z}{2\pi} \left(\frac{k_{\parallel}^2 + P_z k_z}{k_{\parallel}^2 + P_z^2} \right) n_0(k_z - P_z) \delta n(P_z)$$

Note the n_0 factor in the integrand. Thus, the linear term in the dispersion relation is due to structure in the surface.

Feibelman⁴³, developing his earlier RPA theory further, has obtained Eqn. (7) and applies it to a smooth, finite potential barrier—including the Lang-Kohn density profile. He finds that A_1 is finite and not only depends strongly upon diffuseness (i.e., the distance over which the height of the barrier changes) but also is sensitive to the barrier shape. However, in general, A_1 is negative. In particular A_1 equals $-2.5 \text{ eV } \text{\AA}$ for the Lang-Kohn density profile, as compared to $-1.9 \pm 0.6 \text{ eV } \text{\AA}$ in our measurement.

This sensitivity of the linear term of the dispersion to the diffuseness agrees with the numerical conclusion in hydrodynamic models of Bennett⁴⁴, who incorporates a linear surface density profile to approximate the Lang-Kohn density profile, and that of Boardman *et al.*⁴⁵ and Forstmann and Stenschke⁴⁶, who assume a double step-function for the electron density profile. The advantage of such models is the convenient form of the dispersion equation in which the basic parameters can be varied until a best fit to the experimental results is obtained. Figure 21 shows the fits by Bennett and Forstmann and Stenschke for polycrystalline Mg and Al samples in the high energy electron transmission experiments. We see the agreement between the theoretical fits and experimental curve is fairly good. The electron density falls off in the range of 2 to 4 \AA .

Figure 21 also shows the dispersion curve at small k_{\parallel} region ($\lesssim 0.1 \text{ \AA}^{-1}$), using the linear coefficient computed by Feibelman for

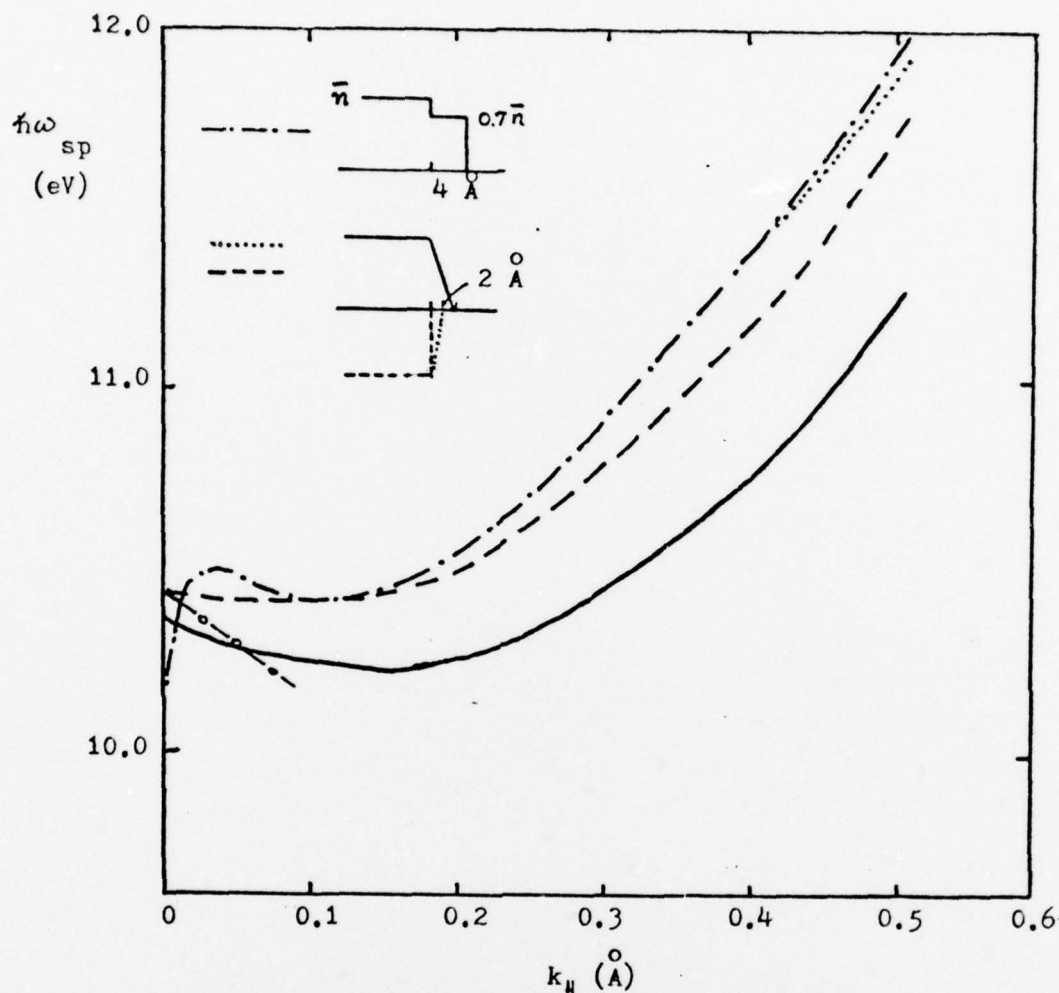


Fig. 21

Comparison of the least-square fit of the surface plasmon dispersion relation of Al(100) with the best fits of the hydrodynamic models to polycrystalline aluminum and magnesium data.

- · - · - Forstmann and Stenschke (Al)⁴⁶
- · · · · Bennett (Mg); different positive charge density
- - - - - profile for the same electron density profile (see the insert)⁴⁴

Also shown is the dispersion at small $k_{||}$ region from Feibelman's RPA calculation of the linear coefficient for the Lang-Kohn density profile.⁴⁷

- · - ·

the Lang-Kohn density profile ($A_1 = -2.5 \text{ eV } \text{\AA}^{-1}$). The agreement with experiment is reasonably good in this region. However, higher order terms in $k_{||}$ have not been calculated in the RPA approach using a realistic density profile like the Lang-Kohn profile. Hence, comparison between experiments and RPA calculations can be only qualitative. The negative sign of A_1 is established among the experiments and calculations. Therefore, in the context of the general relation of Harris and Griffin, Eqn. (7), the surface charge fluctuation, resulting in surface plasmons, occurs at a position which is not symmetrical about the surface $z = 0$ (where $z = 0$ is defined through the vanishing of the second term in Eqn.(7)), but somewhere inside the metal.

Even though the agreement of the two hydrodynamic calculations with experiments is good, there are serious reservations about their validity. The very use of a hydrodynamic formulation means that the electron-hole pairs are left out, and hence collisionless (Landau) damping has been omitted, even though a surface plasmon, unlike a bulk plasmon, can suffer Landau damping at all wave numbers.⁴⁸ Because the rapid spatial variation in the z direction gives rise to Fourier components with large values of the perpendicular wave vector, collisionless damping can still occur for small values of $k_{||}$. Nevertheless, experimentally, the line width of the surface plasmons peak is small enough up to $k_{||} \lesssim 0.5 \text{ \AA}^{-1}$ so that the concept of quasi-particle is still applicable.

Apart from the omission of damping, the application of hydrodynamics to metals can be criticized on the ground that the true hydrodynamic condition, i.e., that the frequency with which the plasma changes is much less than the collision frequency, is not appropriate to the metallic surface because of the low electron density in the tail region of the electron distri-

bution. A hydrodynamic condition, in other words, requires the carrier distribution to relax extremely rapidly, via collisions, to local equilibrium⁴⁵.

However, one can raise the same kind of objection to the use of RPA theories, because RPA theories are strictly applicable only to a high density infinite electron gas model; but, the electron density goes to zero in the tail region at some distance from the surface.

CONCLUSIONS

(1) There are now two independent experimental determinations of SPDR on Al(100), which agree with each other within the experimental uncertainties. Even though various model calculations embody different technical approximations, the consequences of which cannot be separated from those of the models themselves, we can rule out all calculations which use infinite or single step-function density profiles at the surface.

(2) The experimental results demonstrate that models which embody an adequate description of the electron charge density profile and also include the effect of the ion lattice are essential to describe the SPDR and other surface properties, for example, surface energy, on different single crystal faces.

(3) Because the measured dispersion relation cannot be as accurate as we would like in the low k_{\parallel} region due to the finite angular resolution, model calculations of the linear term in SPDR alone are destined for an inconclusive verification. Higher order terms, at least the quadratic term, are needed.

The negative sign of A_1 is established by the experiments and calculations. In the context of the general formula for A_1 given by Harris and Griffin, which relates the linear coefficient A_1 in the surface plasmon dispersion relation to the charge dipole associated with the density fluctuation of surface plasmons, the surface charge fluctuation occurs inside the metal, rather than symmetrically about the surface.

APPENDIX - OXYGEN ADSORPTION ON Al(100)

Introduction

In the course of measuring the surface plasmon dispersion relation (SPDR) for Al(100), we find that when the aluminum single crystal surface is not sufficiently cleaned by argon ion bombardment, the SPDR is modified markedly from that of clean aluminum. Qualitatively, the SPDR first decreases with increasing k_{\parallel} , then stays constant after some cleaning, and finally increases with increasing k_{\parallel} after more cleaning. This effect is presumably due to chemisorbed oxygen and/or a surface oxide. Therefore, we have undertaken to make a quantitative study of the effect of adsorbed oxygen and the growth of oxide on the electronic structure of an aluminum (100) surface.

Experimental Procedure

After the usual cleaning and annealing cycles, an energy loss spectrum of the clean sample was taken. Then oxygen was introduced into the chamber at about 2×10^{-8} Torr. Meanwhile, the pressure was recorded continuously on a chart recorder and the dosage of oxygen was determined from the area under the pressure-time curve in units of Langmuir (10^{-6} Torr-second). During the experiment, the emission current of the gauge was decreased by one order of magnitude. The electron gun was also turned off before oxygen was introduced into the chamber. This procedure eliminated the problem of oxygen poisoning of the electron gun cathode with a resultant decrease in incident current. After some appropriate dosage of oxygen, the leak valve was closed, the chamber was evacuated, and the gun was turned on again.

As in our previous study, the incident and the scattered electron beams were at a glancing angle (12° in specular reflection) to the surface to maximize the information from the surface and at the same time minimize complicating effects from multiple scattering in the bulk crystal.

Spectra from Adsorbed Oxygen

The spectra in Fig. 22 show that the intensity of the 10.3 eV peak, associated with the surface plasmon of clean Al, decreases steadily with exposure. This peak eventually disappears completely at ~ 250 L. Before the disappearance of the 10.3 eV peak, the second peak appears at 7.5 ± 0.2 eV after exposure of about 100 L. This peak is related to the oxygen-aluminum interface because its intensity increases to a maximum and then decreases at higher exposure, which prevents emission of electrons at the oxygen-aluminum interface. The energies of the 10.3 eV and the 7.5 eV peaks are independent of oxygen dosage and also independent of each other, i.e., there is no continuous transition from one peak to the other. Figure 23 shows the intensity variation of these peaks as well as the elastic peak which stays constant in intensity.

Figure 24 shows an energy loss spectrum over a wider range of energy loss and with better statistics after an exposure of 250 L. There is an additional broad peak at 20.6 ± 0.5 eV, which is a characteristic of the sample before cleaning by ion bombardment, and an indication of a small peak at 9.6 eV.

At larger angles of specular reflection, for example, 35° compared with 9° , the 7.5 eV peak disappears and the volume plasmon appears at 15.4 eV (Fig. 25). This is a very clear demonstration of the greater

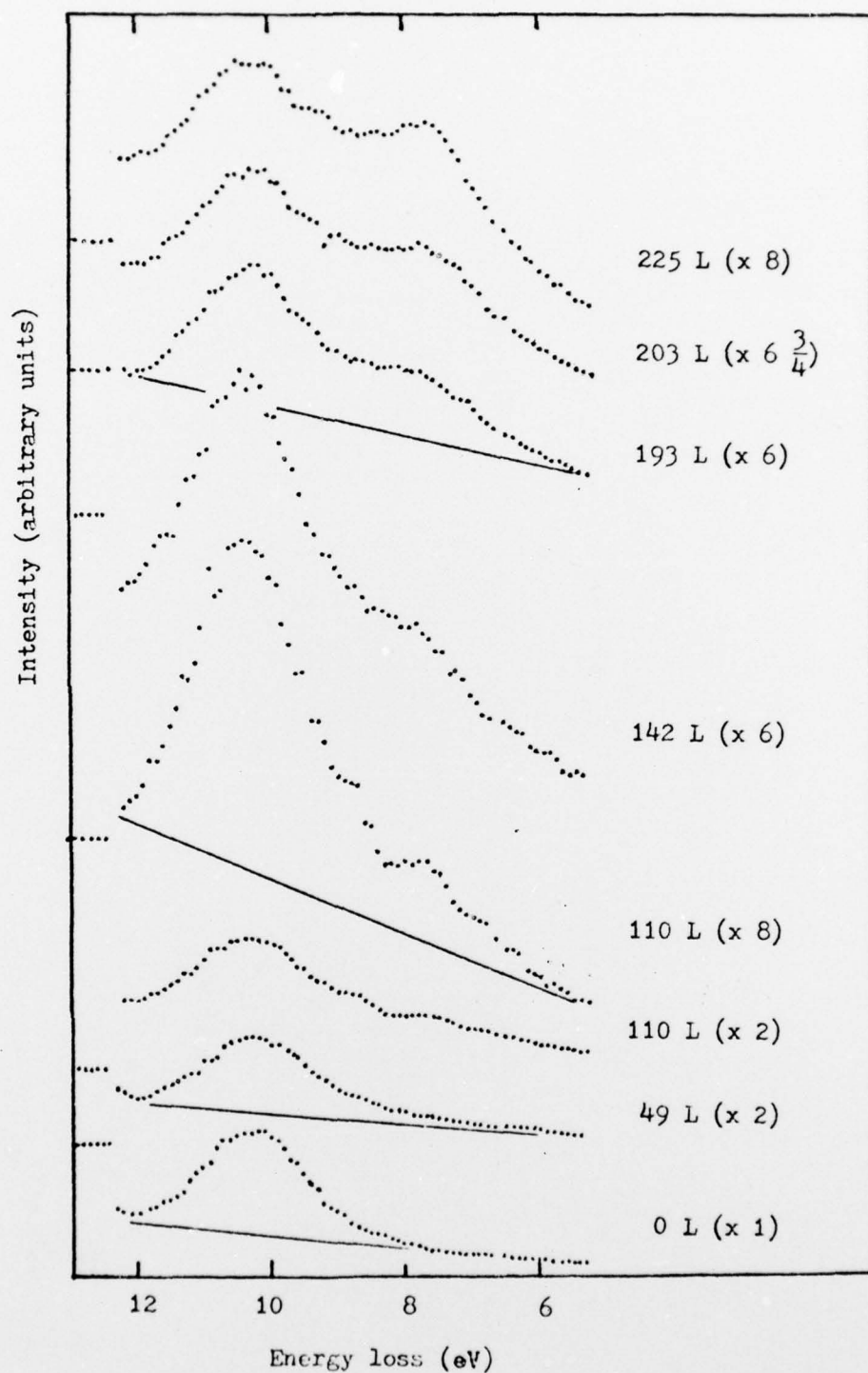


Fig. 22

Energy loss spectra with increasing oxygen exposure. Specular reflection at 12° from the surface. The number in parenthesis indicates the scale factor relative to the spectrum of clean Al. The straight lines are drawn to indicate the background subtraction for Fig. 23.

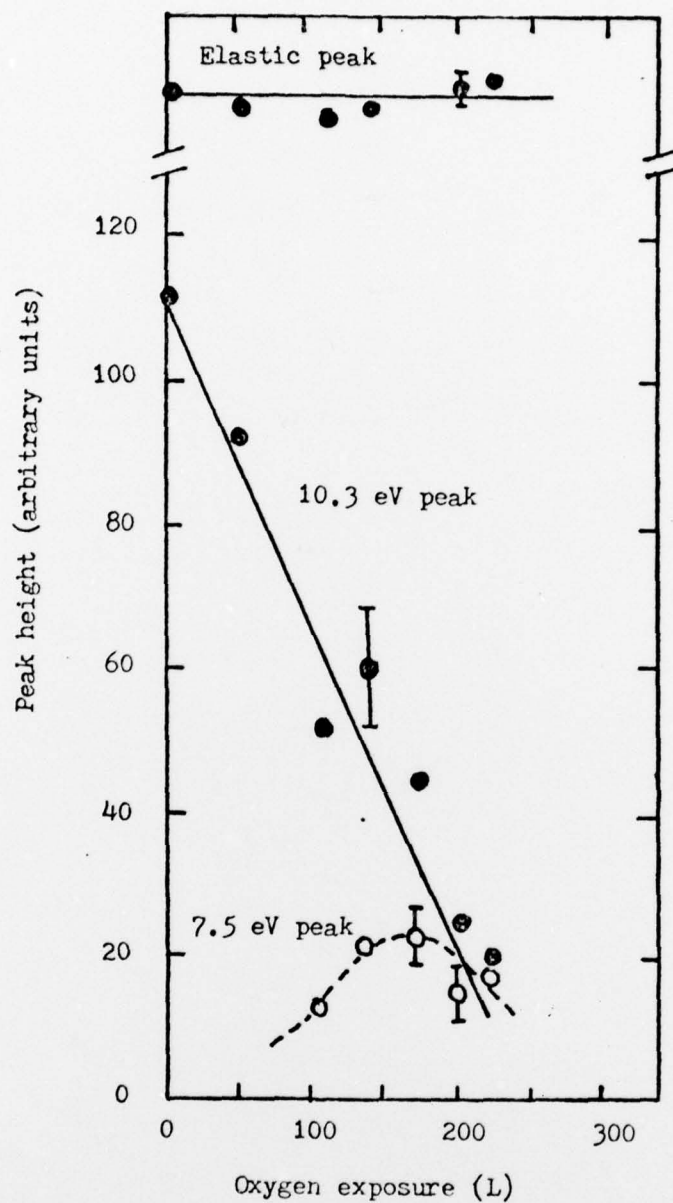


Fig. 23

Peak height of the elastic peak, surface plasmon peak and the 7.5 eV peak as a function of oxygen exposure in Langmuirs (L).

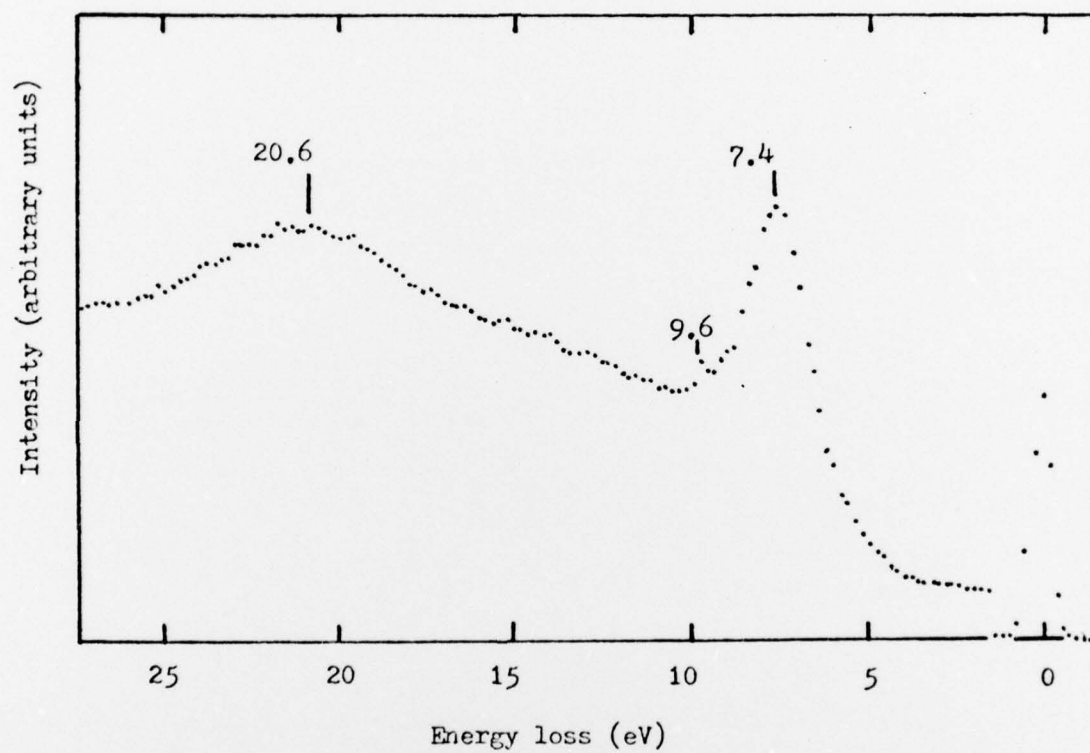


Fig. 24 Energy loss spectrum with wider energy-loss range and better statistics relative to those of Fig. 22.

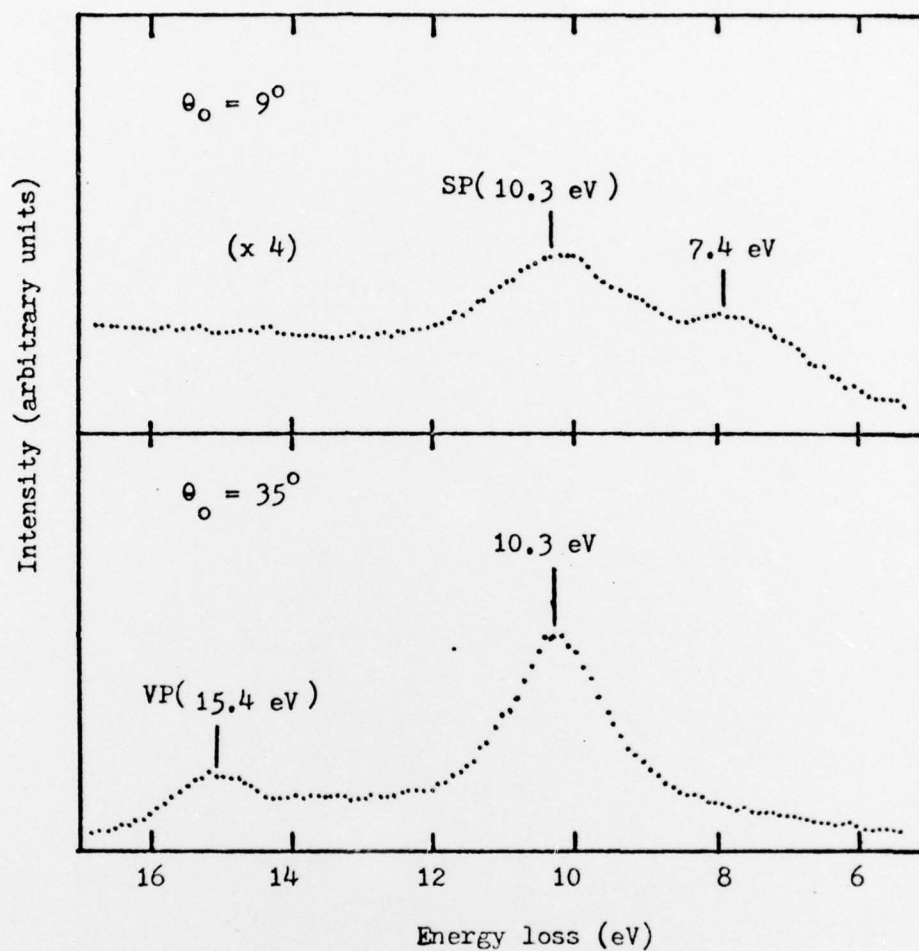


Fig. 25

Energy loss profile at different angles of incidence. Oxygen exposure 67 L and 10 hours in vacuum. The 7.4 eV peak is apparent at glancing incidence, but is absent at higher angle of incidence.

sensitivity to surface condition at glancing incidence relative to normal incidence.

Spectrum (a) in Fig. 26 was obtained with oxygen exposure ~ 200 L. After one hour of heating the sample at 150°C , we obtained spectrum (b), which is not very different from (a). Then we left the sample overnight to obtain spectrum (c). In spectrum (c) the 7.5 eV peak height is higher than the 10.3 eV peak. This indicates that during the overnight period some ambient gas in the chamber (CO , H_2O) adsorbed on the clean surface. However, they are weakly bound because after heating the sample at 200°C for 20 minutes we obtained spectrum (d) where the 10.3 eV peak is higher than the 7.5 eV peak. To test a proposed idea that the surface oxide grows across the surface area from nucleation centers formed at room temperature, the oxidized sample was heated to about 200°C . Spectra (d) to (h) in Fig. 26 show that upon heating the sample the intensity of 10.3 eV peak from the clean surface decreases in time relative to the 7.5 eV peak from islands of oxygen-covered surface until only the latter peak is present, indicating that the surface is uniformly covered with oxygen.

The surface plasmon dispersion relation was also measured up to $k_{\parallel} = 0.33 \text{ \AA}^{-1}$ during oxygen exposure and was found to be constant in energy until the 10.3 eV peak disappears from the spectrum after large exposures to oxygen. The flat dispersion is consistent with the fact that oxygen is more electronegative and, upon adsorbing on the surface, acquires some negative charge, i.e., some electrons from Al atoms are involved in bonding oxygen atoms. Hence, there are fewer electrons at the surface to participate in the collective surface plasma oscillation, and the decrease in dispersion due to electron density fall-off is much more pronounced. The resulting plateau is longer. However, the flat dispersion curve may

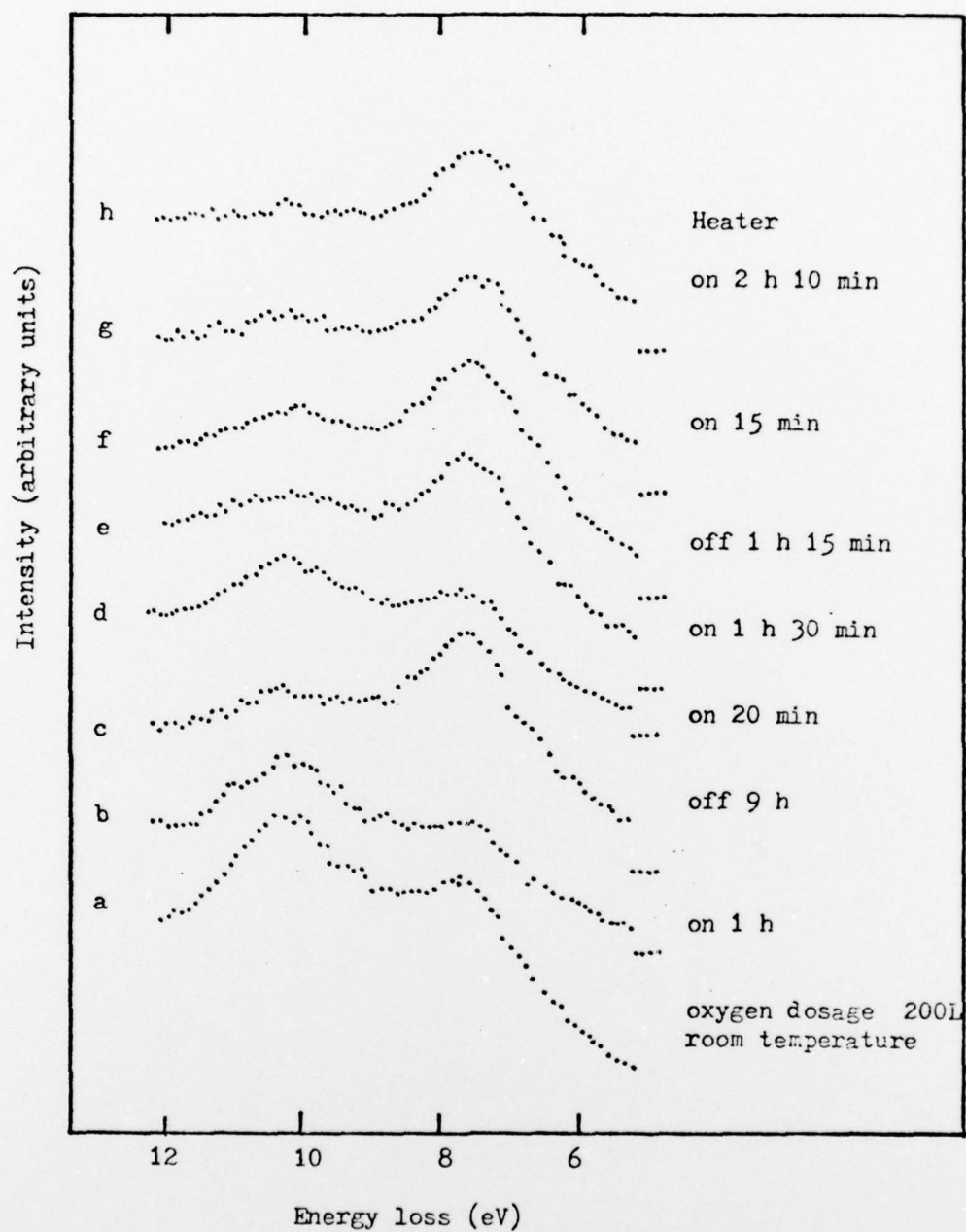


Fig. 26

The effect of heating the sample at 200°C.

also be due to the fact that the intensity of incoherent inelastic scattering from the oxygen atoms forming an amorphous submonolayer on the surface is larger than the coherent inelastic scattering from the single crystal aluminum substrate.

Discussion

Two ELS studies of oxygen adsorbed on single crystal aluminum have been made previously, one by Bradshaw *et al.*⁴⁹ on Al(111) and one on Al(100) by Allié *et al.*⁵⁰. These measurements are made between normal incidence and 45° to the surface.

The simultaneous appearance of 10.3 eV and 7.5 eV peaks at intermediate oxygen exposures (Fig. 22) agrees with some ELS experiments on Al⁵¹⁻⁵³, but disagrees with some other experiments^{54,55}, in which the 10.3 eV peak shifts continuously to 7.5 eV as oxygen is introduced. The behavior of peak intensities at 10.3 eV and 7.5 eV (Fig. 23) is in qualitative agreement with data obtained by Powell and Swan⁵¹. The simultaneous presence of both peaks as well as evidence from the effect of annealing at 200°C (Fig. 26) indicate that there are clusters of chemisorbed oxygen on the surface⁵² so that the incident electrons sample simultaneously both a clean area and an oxygen-covered area. This conclusion is further supported by Auger electron spectroscopy and work function measurements for the (100), (110), and (111) faces of Al by Gartland⁵⁶ who proposes that oxygen atoms adsorb randomly on Al(111) but form islands on the (100) face.

There are two possible explanations for the origin of the 7.5 eV peak. One is that the 7.5 eV peak is an interface plasmon between Al and a dielectric layer of aluminum oxide. Stern and Ferrell⁵⁷ propose that the presence of a thin film of aluminum oxide modifies the surface plasmon

energy of $\hbar\omega_p / \sqrt{2}$ into $\hbar\omega_p / \sqrt{1 + \epsilon}$ where ϵ is the dielectric constant of the surface oxide, which is then calculated to be 3.65, using 15.4 eV for the volume plasmon energy and 7.2 eV for the low-lying loss energy. In our case the low-lying loss energy is 7.5 eV so that ϵ equals 3.2. This value of ϵ is in better agreement with the dielectric constant ($\epsilon = 2.9$) calculated from the relation $n = \sqrt{\epsilon}$, where n is the index of refraction of aluminum oxide at optical frequency ($n = 1.68$). Although the explanation in terms of dielectric constant fits the 7.5 eV peak, the origin of the possible small peak at 9.6 eV and the broad peak at 20.6 eV are not explained. Furthermore, at submonolayer to monolayer coverage (assuming a low sticking coefficient) the concept of dielectric constant, as a macroscopic quantity, is not applicable. Figure 26 shows that there is actually little oxide formation because upon heating the sample at 200°C the 10.3 eV peak disappears and the 7.5 eV peak remains. This experiment indicates that the mobile species is oxygen which chemisorbs on the surface and, upon heating, diffuses over the surface to produce a uniformly covered surface. (However, we cannot rule out the possibility that oxygen desorbs from the graphite heater and deposits on the sample.) Diffusion from an oxide source is unlikely because the bond strength of Al_2O_3 would require a much higher temperature for dissociation. This observation is consistent with a recent photoelectron spectroscopy experiment of Flodström et al.⁵⁵, which shows that there is an intermediate chemisorption phase for oxygen on Al(100) before oxidation.

The alternative explanation for the 7.5 eV peak is that the energy loss structure is due to a single electron transition. ELS provides information not only about the collective features of conduction electrons but also about the interband and intraband single particle transitions,

which involve the densities of initial and final states. Combining ELS with the photoelectron spectroscopy which probes the density of the initial states, we can probe the density of the unfilled, final electron states. Recently, Yu *et al.*⁵⁸ and Flodström *et al.*⁵⁹, using ultraviolet photoelectron spectroscopy (UPS) to study chemisorption of oxygen on Al film, found that a peak at 7.2 eV below the Fermi level of Al appeared at an exposure of only ~ 1 L of oxygen and reached saturation at ~ 50 L. This peak is identified as the O(2p) level. Other photoemission experiments^{54,55,60} give the same results.

A small peak at 9.6 eV was observed in UPS by Flodström *et al.*^{54,59} and Martinsson *et al.*⁶⁰, but not observed in UPS by Yu *et al.*⁵⁸ Martinsson *et al.* observed two peaks at 7 and 9.5 eV below E_F for the (100) face but only the 7 eV peak was observed for the (110) and (111) faces. The origin of this 9.6 eV peak is explained by Messmer and Salahub⁶¹ in their molecular-orbital cluster study of chemisorption of oxygen atoms on Al(100) as due mainly to bonding combinations of in-plane oxygen (p) orbitals with aluminum (s) and (p) orbitals. In the same calculation the 7 eV peak arises from both in-plane and out-of-plane oxygen (p) orbitals in bonding combinations with aluminum orbitals.

In terms of interband transitions the initial state is an oxygen level, the final state is an Al level from the increase and subsequent decrease in intensity as a function of oxygen exposure (Fig. 23). Benndorf *et al.*⁵³, in their ELS experiment, cannot decide whether the spectral structure at 7.5 eV is a peak or a step, and they suggest the 7.5 eV structure is due to the interband transition from the O(2p) level to the empty conduction band of Al. If the final state were the unoccupied conduction band of Al, the ELS spectra would show a step near 7.2 eV, instead of a sharp peak. Because we see clearly in our spectrum (Fig. 24) a well-defined

peak at 7.5 eV (FWHM \sim 3 eV), the final state is a well-defined yet unidentified state near E_F of Al.

Among various ELS experiments there is disagreement on the position of the broad peak at high oxygen exposures. Powell and Swan⁵¹ observe the broad peak at 22.2 eV, Benndorf *et al.*⁵³ at 19.2 eV, and this experiment at 20.6 eV. This situation makes the interpretation of the origin of this broad peak difficult. These values are all lower than the energy of O(2s) level in an oxide, which is at 23.6 eV below E_F of Al in the x-ray photoelectron spectrum⁴⁹. However, because the glancing geometry in our experiment excludes bulk effects, we have demonstrated that this broad peak has a surface origin.

CONCLUSIONS CONCERNING OXYGEN ADSORPTION

In summary we have shown that the 7.5 eV peak is sharp and that there may be a small peak at 9.6 eV, so far unseen in other ELS experiments. Two interpretations for the 7.5 eV peak are given, in terms of dielectric constant and interband transition. To distinguish between these two interpretations, we suggest that final-state spectroscopy by synchrotron radiation, which probes the density of the empty states above the Fermi level, could be employed to determine whether there is a well-defined empty state just above the E_F of Al which may be the final state of the 7.5 eV transition from O(2p) level. The broad peak at \sim 21 eV in our experiment is shown to originate at the surface.

REFERENCES

1. V. Celli, lectures presented at an International Course, Pt. I, Trieste, Italy, 16 Jan. - 10 April 1974 (Vienna, Austria: IAEA, 1975) pp. 393-422.
2. D. Pines and D. Bohm, Phys. Rev. 85, 338 (1952).
3. R. H. Ritchie, Phys. Rev. 106, 874 (1957).
4. C. J. Powell and J. B. Swan, Phys. Rev. 115, 869 (1959); 116, 81 (1959).
5. P. J. Feibelman, Phys. Rev. B3, 220 (1971).
6. A. D. Boardman, B. V. Paranjape and R. Teshima, Phys. Lett. 48A, 327 (1974).
7. D. E. Beck and B. B. Dasgupta, Phys. Rev. B12, 2592 (1970).
8. J. Harris and A. Griffin, Can. J. Phys. 48, 2592 (1970).
9. T. Kloos and H. Raether, Phys. Lett. 44A, 157 (1973).
10. K. J. Frane and H. Raether, Phys. Rev. Lett. 37, 1355 (1976).
11. C. B. Duke, L. Pietronero, J. O. Porteus and J. F. Wendelken, Phys. Rev. B12, 4059 (1975).
12. C. B. Duke and A. Bagchi, J. Vac. Sci. Technol. 9, 738 (1972).
13. C. B. Duke and U. Landman, Phys. Rev. B7, 1368 (1973).
14. C. B. Duke and U. Landman, Phys. Rev. B8, 505 (1973).
15. J. O. Porteus and W. N. Faith, J. Vac. Sci. Technol. 9, 1062 (1972).
16. J. O. Porteus and W. N. Faith, Phys. Rev. 8, 491 (1973).
17. J. O. Porteus and W. N. Faith, Phys. Rev. B12, 2097 (1975).
18. J. Wendelken, U. of Illinois, Ph.D. Thesis (1974); Coordinated Science Lab. Report R-667.
19. E. A. Stern and R. A. Ferrell, Phys. Rev. 120, 130 (1960).
20. Y. Murata and S. Ohtani, J. Vac. Sci. Technol. 9, 789 (1972).

21. E. M. Purcell, Phys. Rev. 54, 818 (1938).
22. M. J. W. Boness and G. J. Schulz, Phys. Rev. A9, 1969 (1974).
23. J. A. Simpson, Rev. Sci. Instrum. 35, 1698 (1964).
24. C. E. Kuyatt and J. A. Simpson, Rev. Sci. Instrum. 38, 103 (1967).
25. W. A. Fraser, J. V. Florio, W. N. Delgass and W. D. Robertson, Rev. Sci. Instrum. 44, 1490 (1973).
26. J. M. Burkstrand, Ph.D. Thesis, Univ. of Illinois (1972); Coordinated Science Laboratory Report R-544.
27. M. R. Feinstein, Ph.D. Thesis, Yale University (1977).
28. C. B. Duke, L. Pietronero, J. O. Porteus, and J. F. Wendelken, Phys. Rev. B12, 4059 (1975).
29. K. J. Krane and H. Raether, Phys. Rev. Lett. 37, 1355 (1976).
30. C. B. Duke and U. Landman, Phys. Rev. B8, 505 (1973).
31. J. O. Porteus and W. N. Faith, Phys. Rev. B12, 2097 (1975).
32. J. F. Wendelken, Phys. D. Thesis, University of Illinois (1974); Report R-667, Coordinated Science Laboratory, University of Illinois.
33. J. O. Porteus and W. N. Faith, Phys. Rev. B8, 491 (1973).
34. P. J. Feibelman, Phys. Rev. 176, 551 (1968).
35. D. M. Newns, Phys. Rev. B1, 3304 (1970).
36. D. E. Beck, Phys. Rev. B4, 1555 (1971).
37. Ch. Heger and D. Wagner, Phys. Lett. 34A, 448 (1971).
38. D. E. Beck and V. Celli, Surf. Sci. 37, 48 (1973).
39. R. H. Ritchie and A. L. Marusak, Surf. Sci. 4, 234 (1966).
40. J. Heinrichs, Phys. Rev. B7, 3487 (1973).
41. R. H. Ritchie, Progr. Theoret. Phys. (Kyoto) 29, 607 (1963).
42. J. Harris and A. Griffin, Phys. Lett. 34A, 51 (1971).
43. P. J. Feibelman, Phys. Rev. Lett. 30, 975 (1973).

44. A. J. Bennett, Phys. Rev. B1, 203 (1970).
45. A. D. Boardman, B. V. Paranjape, and R. Teshima, Surf. Sci. 49, 275 (1975).
46. F. Forstmann and H. Stenschke, Phys. Rev. B17, 1489 (1978).
47. N. D. Lang and W. Kohn, Phys. Rev. B1, 4555 (1970).
48. A. Eguiluz and J. J. Quinn, Phys. Rev. B15, 1347 (1976).
49. A. M. Bradshaw, P. Hofmann and W. Wyrobisch, Surf. Sci. 68, 269 (1977).
50. G. Allié, E. Blanc, D. Dufayard and P. Haymann, Surf. Sci. 47, 635 (1975).
51. C. J. Powell and J. B. Swan, Phys. Rev. 118, 640 (1960).
52. Y. Murata and S. Ohtani, J. Vac. Sci. Technol. 9, 789 (1972).
53. C. Benndorf, G. Keller, H. Seidel and F. Thieme, Surf. Sci. 67, 589 (1977).
54. S. A. Flodström, L.-G. Petersson, and S. B. M. Hagström, Solid State Commun. 19, 257 (1976).
55. S. A. Flodström, R. Z. Bachrach, R. S. Bauer, And S. B. M. Hagström, Phys. Rev. Lett. 37, 1282 (1976).
56. P. O. Gartland, Surf. Sci. 62, 183 (1977).
57. E. A. Stern and R. A. Ferrell, Phys. Rev. 120, 130 (1960).
58. K. Y. Yu, J. N. Miller, P. Chye and W. E. Spicer, Phys. Rev. B14, 1446 (1976).
59. S. A. Flodström, L.-G. Petersson and S. B. M. Hagström, J. Vac. Sci. Technol. 13, 280 (1976).
60. C. Martinsson, L.-G. Petersson, S. A. Flodström, and S. B. M. Hagström, in Proceedings of the International Study Conference on Photoemission from Surfaces, Noordwijk, Holland, September 13-16 (1976); unpublished.
61. R. P. Messmer and D. R. Salahab, Phys. Rev. B16, 3415 (1977).